THE JOURNAL OF
PHYSICAL
CHEMISTRY
A

VOLUME 107, NUMBER 42, OCTOBER 23, 2003

REVIEW ARTICLE

Photophysical Properties of Directly Linked Linear Porphyrin Arrays

Dongho Kim*

National Creative Research Initiatives Center for Ultrafast Optical Characteristics Control and Department of Chemistry, Yonsei University, Seoul 120-749, Korea

Atsuhiro Osuka*

Department of Chemistry and Core Research for Evolutional Science and Technology (CREST), Japan Science and Technology Corporation, Kyoto University, Kyoto 606-8502, Japan

Received: April 22, 2003; In Final Form: June 24, 2003

A variety of porphyrin arrays connected by diverse linkers have been envisaged and prepared for the applications in molecular photonics and electronics. From a viewpoint of operational requirements, the porphyrin arrays should have the very regular pigment arrangements which allow a facile light energy or charge flow along the arrays but do not result in the alteration of individual properties of the constituent pigments leading to formation of so-called energy or charge sink. In these respects, the directly coupled (orthogonal and fused) porphyrin arrays without any linkers are ideal, because the conformational heterogeneity mainly arising from a dihedral angle distribution between the neighboring porphyrin moieties should be minimized. In addition, the electronic effect of the linker can be disregarded in design strategy of molecular photonic devices, because the linker can also be considered as a transmission element in electronic communication. Considering these features, these types (orthogonal vs fused) of porphyrin arrays would be one of the most suitable synthetic molecular modules for the realization of molecular photonic and electronic devices. To unveil the functionalities of various porphyrin arrays, starting from the dihedral angle dependence on the photophysical properties of the porphyrin dimers, we have extended our knowledge to longer orthogonal and fused porphyrin arrays. Overall, the regularly arranged porphyrin arrays with ample electronic interactions will be promising in the applications such as molecular wires, sensors, optical nonlinear materials, and so on.

I. Introduction

During the past decade, there have been a variety of trials to mimic the natural photosynthetic system at molecular levels to develop molecular photonic and electronic devices, which is called *molecular electronics*.[1−8] Among numerous molecular pigments for candidates as building block elements in molecular devices, the versatile optical (absorption and emission), redox, and photochemical properties of porphyrins and their derivatives make them ideally suited as components of nanostructures.[9−10]

Continuing efforts to realize the mimicry of solar energy harvesting complexes have enabled the design and synthesis of various types of covalently linked porphyrin arrays with the goal of applying these arrays to molecular photonic and electronic devices. Multi-porphyrin arrays have been constructed using several types of shorter linkers that are suitable for preparing linear or extended architectures via meso position attachment. Various synthetic strategies have been developed

---

* To whom correspondence should be addressed. E-mail:dongho@yonsei.ac.kr. Fax: +82-2-2123-2434. E-mail: osuka@kuchem.kyoto-u.ac.jp

10.1021/jp030490s CCC: $25.00

in order to make multi-porphyrin oligomers with linear, cyclic, and cross-linked geometries, which include porphyrins joined by ethene,[11] ethyne,[12] butadiyne,[12−15] furan,[13] enyne,[15] hexatriene,[16] *p*-phenylene,[17] phenylethene,[18] naphthalene,[19] biphenyl,[19,20] phenanthrene,[19] and ethynylphenylethyne[15] groups.

For the applications as molecular photonic and electronic wires, some requirements should be considered for better performances: (1) ample electronic interactions between neighboring porphyrin pigments for efficient energy transfer, (2) long π-electron conjugation length that enhances charge mobility or optical nonlinearity, (3) well-defined and rigid molecular structures to be void of any energy or charge sink that disrupts the energy or charge flow along the array, (4) a high level of stability and significant solubility for chemical processing, and (5) sufficient length which is long enough for linkage between energy donor and acceptor for energy transfer as a molecular photonic wire or for linkage of a microelectrode as a molecular electric wire.

Recently, there is a remarkable progress in synthesizing capabilities of long rodlike porphyrin arrays in which porphyrin pigments are directly connected together through meso positions up to 128 units without any linkers (Z*n*, $n = 1, 2, 3, ..., 128$, orthogonal porphyrin array, Chart 1).[21] The overall orthogonal conformation between the adjacent porphyrin units in the orthogonal porphyrin arrays disrupts π-electron conjugation over the array despite of the very short interporphyrin distance of 8.35 Å.[22] In this regard, the directly linked orthogonal porphyrin arrays could provide the prospects as artificial light harvesting arrays and molecular photonic wires because the unique photophysical aspect of these molecular arrays arising from substantial interchromophoric electronic interactions mimics the facile energy migration processes in biological light harvesting assemblies, where electronic delocalization is negligible due to a lack of direct bond linkage between individual pigment molecules.[22]

A successful preparation of long porphyrin arrays raises fundamental questions regarding exciton coupling, π-electron delocalization, and relative orientations between the adjacent porphyrins. As a systematic approach to investigate these interporphyrinic interactions, a control of the dihedral angle of the meso−meso coupled diporphyrins is an intriguing challenge,[23] because it may offer a fine-tuning of electronic interactions between the two porphyrins, which may eventually result in a manipulation of intramolecular excitation energy and electron-transfer processes. The electronic interactions between the adjacent porphyrin moieties in the meso−meso linked porphyrin arrays must be minimum at 90° dihedral angle. Therefore, tilting of porphyrin ring from 90° to < 90° angle causes a symmetry change from D_{2d} to D_2 with a simultaneous increase in the electronic interactions between the porphyrins (the meso−meso linked diporphyrins strapped with a dioxymethylene group: S*n*, $n = 1, 2, 3, 4, 8$, and 10 where *n* is the number of carbon atoms in the chain, Chart 1 and Scheme 1), which may, in turn, alter a variety of photophysical properties depending on the degree of electronic interactions.[23]

Long π-conjugated organic molecules inevitably encounter the ECL (effective conjugation length) effect because of the bond alternation in these molecules.[24] To realize molecular wires as good conducting organic material and simultaneously overcome the ECL effect, the connection of as many porphyrin molecules as possible with a completely flat structure, as long as its synthetic strategy is not so outrageous, should be one of highly plausible candidates such as graphite, which results in the maximization of π-electron conjugation. Up to now, the meso−meso, β-β, β-β triply linked porphyrin arrays up to 12 units (T*n*, $n = 1, 2, 3, ..., 12$, fused porphyrin array, Chart 1) have been successfully prepared.[25] Although the long-chain alkyl groups are attached to increase the solubility, the flat molecular structure still reduces the solubility significantly which is a main obstacle in preparing even longer fused porphyrin arrays.

Based on fundamental understanding of excitonic interactions depending on the dihedral angle in the porphyrin dimers (Sn), we have extended our knowledge on the photophysical properties and molecular architecture relationship to the directly meso−meso linked porphyrin arrays (Z*n*) and the directly meso−meso, β-β, β-β triply linked porphyrin arrays (T*n*). The Z*n* are expected to be utilized not only to position two active centers at a known distance apart and connect them by a medium of known structure for light signal transmission but as an efficient photosensitizer themselves. At the same time, the T*n* are also intriguing not only in view of their potential applications as nonlinear optical materials, infrared (IR) dyes, optical limiters, and optoelectronic devices but also in view of scientific curiosity how such extremely conjugated π-electronic systems behave in their excited states.

II. Experimental Methods

Sample Preparation and Steady-State Spectroscopic Measurements. The details of synthesis of the porphyrin molecular systems studied here were documented in the relevant previous papers.[21,23,25] The absorption spectra were recorded by using a Varian Cary 3 spectrophotometer, and fluorescence measurements were made on a scanning SLM-AMINCO 4800 spectrofluorometer, which makes it possible to obtain the corrected fluorescence spectra using Rhodamine B as a quantum counter. Steady-state fluorescence excitation anisotropy spectra were obtained by changing the detection polarization in the fluorescence path parallel or perpendicular to the polarization of the exciting light. Then anisotropy values were calculated as follows:

$$r = \frac{I_{VV} - GI_{VH}}{I_{VV} + 2GI_{VH}}$$

where I_{VV} (or I_{VH}) is the signal intensity when the excitation light is vertically polarized and only vertically (or horizontally) polarized portion of fluorescence is detected, denoting that the subscripts stand for excitation and detection polarization, respectively. The factor *G* defined by I_{HV}/I_{HH} corresponds to the ratio of the sensitivities of the detection system for vertically and horizontally polarized light.

Transient Absorption Measurement Setup. The dual-beam femtosecond time-resolved transient absorption spectrometer consisted of a self-mode-locked femtosecond Ti:sapphire oscillator (Coherent, MIRA), a Ti:sapphire regenerative amplifier (Clark MXR, CPA-1000) pumped by a Q-switched Nd:YAG laser (Clark MXR, ORC-1000), a pulse stretcher/compressor, OPA (Light Conversion, TOPAS) system, and an optical detection system. A femtosecond Ti:sapphire oscillator pumped by a CW Nd:YVO_4 laser (Coherent, Verdi) produces a train of ∼80 fs mode-locked pulses with an averaged power of 650 mW at 800 nm. The amplified output beam regenerated by chirped pulse amplification (CPA) had ca. 150 fs pulse width and a power of ca. 1 W at 1 kHz repetition rate, which was divided into two parts by a 1:1 beam splitter. One was color-tuned for the pump beam by optical parametric generation and amplification (OPG-OPA) technique. The resulting laser pulse had a temporal width of ∼150 fs in the UV/vis/IR range. The pump

CHART 1

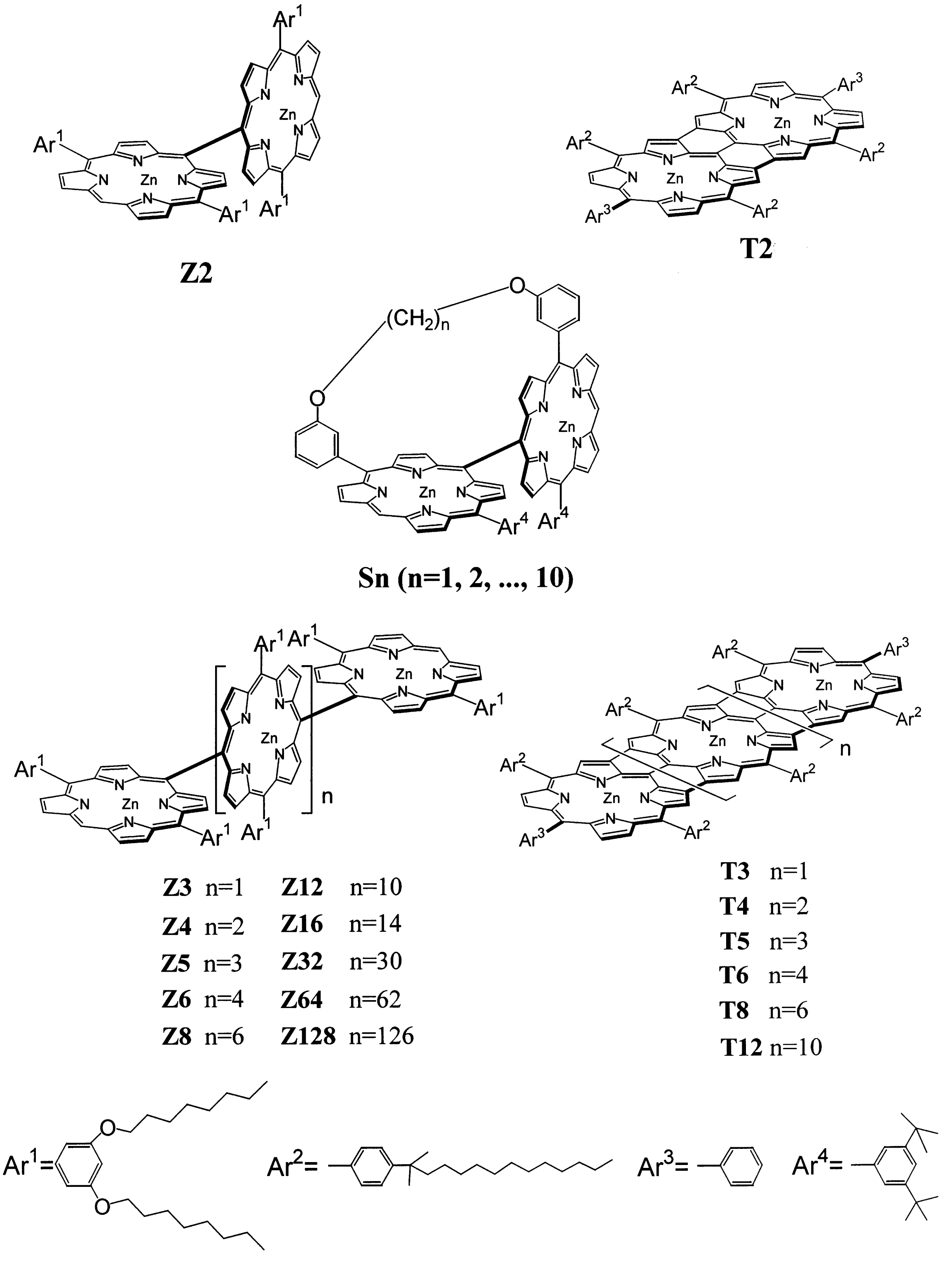

Z2

T2

Sn (n=1, 2, ..., 10)

Z3 n=1
Z4 n=2
Z5 n=3
Z6 n=4
Z8 n=6
Z12 n=10
Z16 n=14
Z32 n=30
Z64 n=62
Z128 n=126

T3 n=1
T4 n=2
T5 n=3
T6 n=4
T8 n=6
T12 n=10

beam was focused to a 1 mm diameter spot, and the laser fluence was adjusted to avoid the damage of sample by using a variable neutral-density filter. The other was focused onto a flowing water cell to generate a white light continuum, which was again split into two parts. The one part of the white light continuum was overlapped with the pump beam at the sample to probe the transient, whereas the other part of the beam was passed through the sample without overlapping the pump beam. The time delay between pump and probe beams was controlled by making pump beam travel along a variable optical delay. The white light continuum beams after the sample were sent to a 15 cm focal length spectrograph (Acton Research) through each optical fiber and then detected by a dual-channel 512 channel photodiode array (Princeton Instruments). The intensity of the white light continuum of each 512 channel photodiode array was processed to calculate the absorption difference spectrum at the desired time delay between pump and probe pulses.

Femtosecond Fluorescence Upconversion Setup. The amplified output of the Ti:sapphire laser is divided by a 1:1 beam splitter into two parts. One of them was frequency-doubled by a 0.5 mm LBO crystal to produce the excitation pulses at 400 nm. The excitation beam was loosely focused onto the sample

SCHEME 1

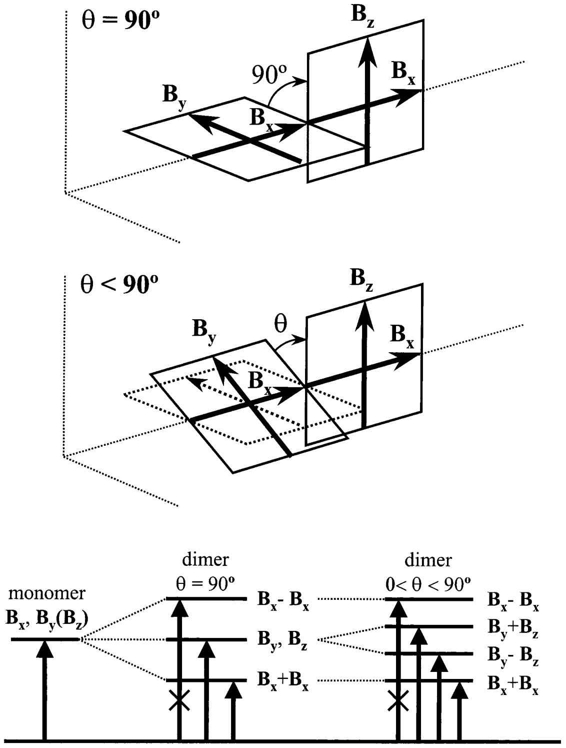

with a spot size of ∼1 mm by a concave mirror. The luminescence was collected and focused onto a 1 mm BBO crystal by two identical parabolic mirrors ($f = 70$ mm, $d = 50$ mm). The other part of the fundamental laser beam was focused onto the BBO crystal with a spatial overlap with the focused emission spot. The time-delay between pump and gate pulses was controlled with a computer-driven optical delay line. The up-converted UV light was focused onto the entrance slit of a monochromator (Jobin-Yvon, HR320). The scattered light was filtered out with a combination of pinhole and appropriate color filters. The instrumental response was estimated to be ∼250 fs from the cross-correlation function between pump and gate beams. The output current from a photomultiplier tube (Hamamatsu) was amplified with a fast preamplifier, and then the output voltage was fed into a Boxcar averager (SR250). The resultant signal modulated by a chopper was phase-sensitively measured by a lock-in-amplifier (EG&G) and then fed into a personal computer for further data processing. Much care was taken to avoid a possible saturation of photomultiplier tube due to the short duration of up-converted UV light even though its average power is very low.

Time-Correlated Single Photon Counting Technique. Picosecond time-resolved fluorescence experiments were carried out by using the time-correlated single photon counting (TCSPC) method. The picosecond excitation pulses were obtained from a cavity-dumped picosecond dye laser (Coherent 702) synchronously pumped by a mode-locked Nd:YAG laser (Coherent Antares 76-s). The cavity-dumped beam from the dye laser had 2 ps pulse width and an average power of ca. 40 mW at 3.8 MHz dumping rate when Rhodamine 6G as the gain dye was used. The emission was collected at 45° with respect to the excitation laser beam by 5- and 25-cm focal length lenses, focused onto a monochromator (Jobin-Yvon HR320), and detected with a microchannel plate photomultiplier tube (Hamamatsu R2809U). The signal was amplified by a wideband amplifier (Philip Scientific); sent to a Quad constant fraction discriminator (Tennelec), a time-to-amplitude converter (Tennelec), a counter (Ortec), and a multichannel analyzer (Tennelec/Nucleus); and stored in a computer.

Raman Spectroscopic Measurements. The ground-state resonance Raman spectra of various porphyrin molecules were obtained by photoexcitation using a cw Ar ion laser (Coherent INNOVA 90) and a cw Kr ion laser (Coherent INNOVA 70K). Raman scattering signals were collected in a 90° scattering geometry. Various Raman detection systems were used such as a 1-m double monochromator (ISA Jobin-Yvon U-1000) equipped with a thermoelectrically cooled photomultiplier tube (Hamamatsu R943−02), a single pass spectrograph (Acton Research 500i) equipped with a charge-coupled device (PI LN/CCD-1152E). The vibrational normal modes of porphyrin monomers have been extensively studied experimentally and theoretically. Spiro et al. have provided normal-mode analyses of nickel tetraphenylporphyrin ($Ni^{II}TPP$)[26] and nickel octaethylporphyrin ($Ni^{II}OEP$)[27] based on the isotope frequency shifts and normal mode calculations with the GF matrix method and a valence force field using semiempirical parameters. In the present work, we adopted the B3LYP hybrid density-functional theory as implemented in the Gaussian 98 suite of programs[28] to calculate the optimized geometry and normal modes of the fused porphyrin arrays. The basis set used is the 6-31G set for carbon, nitrogen, and hydrogen atoms, and Huzinaga's (14s8p5d) set contracted to [5s3p2d] for Zn.

III. Photophysical Properties of Orthogonal Porphyrin Arrays: Z*n*

Steady-State Absorption Spectra of Orthogonal Porphyrin Arrays. It has been well established that there is a relatively large energy separation in metalloporphyrin monomers between the S_2 (B band) and S_1 (Q band) states. These two states are considered as a 50−50 admixture of two excited electronic configurations $^1(a_{1u},e_g)$ and $^1(a_{2u},e_g)$ in accidental degeneracy, and the potential energy surfaces of the S_1 and S_2 states are almost parallel especially in meso-aryl-substituted porphyrin monomers. The absorption spectra of the directly linked Zn(II) porphyrin arrays normalized at 413 nm which corresponds to the high-energy Soret bands are shown in Figure 1a. As reported previously,[22] the meso−meso-coupled porphyrin arrays displayed split Soret bands due to exciton coupling. With an increase in the number of porphyrin units, the low-energy Soret band is red-shifted, whereas the high-energy Soret band remains nearly unchanged, resulting in a progressive increase in the splitting energy. The relative intensities of split Soret bands also depend on the number of porphyrin units; the intensity of the low-energy Soret bands becomes increasingly stronger than that of the high-energy Soret bands. On the other hand, the spectral shifts in the Q band region are modest with a gradual increase in intensity. Figure 1b shows the absorption spectra of the arrays with absolute intensity, which may be helpful for recognizing the high absorptivity of longer arrays such as Z64. As the number of porphyrin units increases, the extinction coefficients are much enhanced up to $>10^6$ M^{-1} cm^{-1} for Z64 covering almost entire visible region. The large extinction coefficients as well as the wide spectral coverage in longer porphyrin arrays provide a prospect that the directly linked porphyrin arrays can be good candidates as the artificial light harvesting complexes to capture efficiently a wide range of the incident visible light.

The systematic spectral changes of the Soret bands can be explained by the point-dipole exciton coupling theory developed by Kasha.[29−31] The Soret band of Zn(II) porphyrin has two perpendicular dipole components of B_x and B_y, as depicted in Scheme 1, which are degenerate in a simple monomer. However,

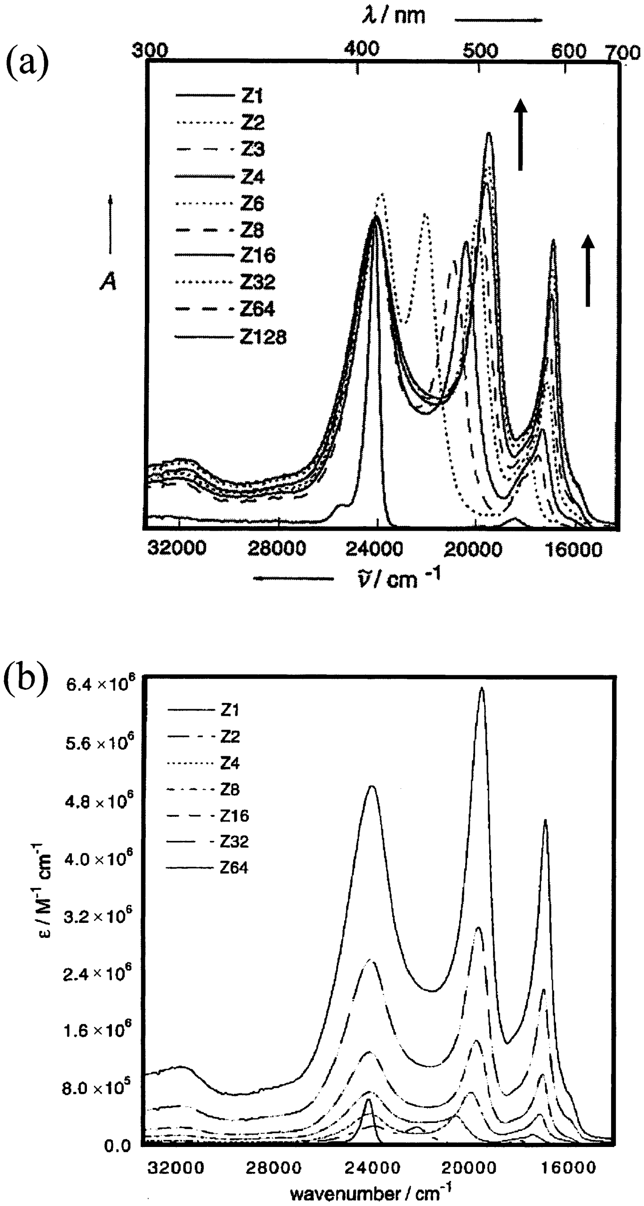

Figure 1. (a) Ultraviolet−visible-infrared absorption spectra of porphyrin monomer and meso−meso-linked porphyrin arrays from Z2 to Z128. (b) A series of extinction coefficient spectra of the porphyrin arrays up to Z64 in THF. Reproduced with permission from ref 22b.

in the case of Z2, parallel B_x transitions couple effectively, whereas other dipole interactions should be virtually zero for an averaged perpendicular conformation in Z2. Thus, the Soret band of Z2 is split into a red-shifted B_x component and unperturbed B_y and B_z components (Scheme 1). Though the unperturbed Soret transitions observed around 413 nm for all of the arrays (Z2−Z128) suggest an orthogonal conformation, we note that these bands also become broader as the porphyrin arrays become longer, indicating the increasing conformational heterogeneities caused by the dihedral angle distribution, aggregate formation, and partial insolubility, if any, of longer porphyrin arrays.

Electronic Coupling Strength of Orthogonal Porphyrin Arrays. According to the exciton coupling theory,[29−31] the relationship of the splitting energy, ΔE, is predicted as

$$\Delta E = 2V\cos\left(\frac{\pi}{N+1}\right) \qquad (1)$$

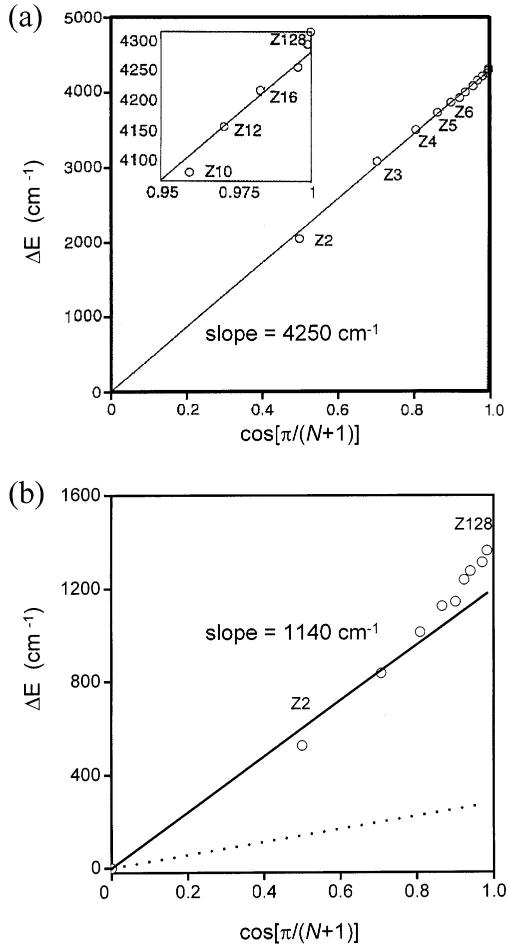

Figure 2. (a) Plot of the energy differences between the high-energy Soret band and the low-energy Soret band as a function of the number of porphyrin units in the Z*n*. (b) The energy differences between Q(1,0) bands of Z*n* and that of Z1 as a function of the number of porphyrin units. The fitted lines are simulated by the eq 1 with $V = 570$ cm^{-1} (solid line) and $V = 280$ cm^{-1} (dashed line). Reproduced with permission from ref 22b.

where N represents the number of porphyrin units and V is the coupling strength.[32] The splitting energy can be determined by the energy difference between the red-shifted B_x bands and the unperturbed B_y and B_z bands. When ΔE data were plotted according to eq 1, we obtained a straight line with a slope of 4250 cm^{-1} ($V = 2125$ cm^{-1}) as shown in Figure 2a. The observed linear relationship indicates that the absorption spectral shapes are actually influenced by the number of porphyrin units, and the constituent porphyrin pigments are aligned in a regular arrangement though some deviation from the linearity was observed in the region of very long arrays.

In a similar analogy, the exciton coupling strength in the S_1 state was evaluated. The energy differences between the Q(1,0) bands of Z1 and the porphyrin arrays (Z2−Z16) were plotted according to eq 1. We obtained the best-fitted lines with a slope of 1140 cm^{-1} ($V = 570$ cm^{-1}) as shown in Figure 2b (solid line). If the electronic coupling between porphyrin units is totally attributed to the dipole−dipole interaction, V can be estimated to be ~130 cm^{-1} from the ratio of the integrated absorption area between the B and Q bands (~1/16), and the consequent energy differences can be predicted as the dotted line in Figure 2b, which is much deviated from the experimental values, indicating that there are additional interactions besides the point dipole−dipole interaction. These additional interactions are attributable to the through-bond interaction between porphyrin

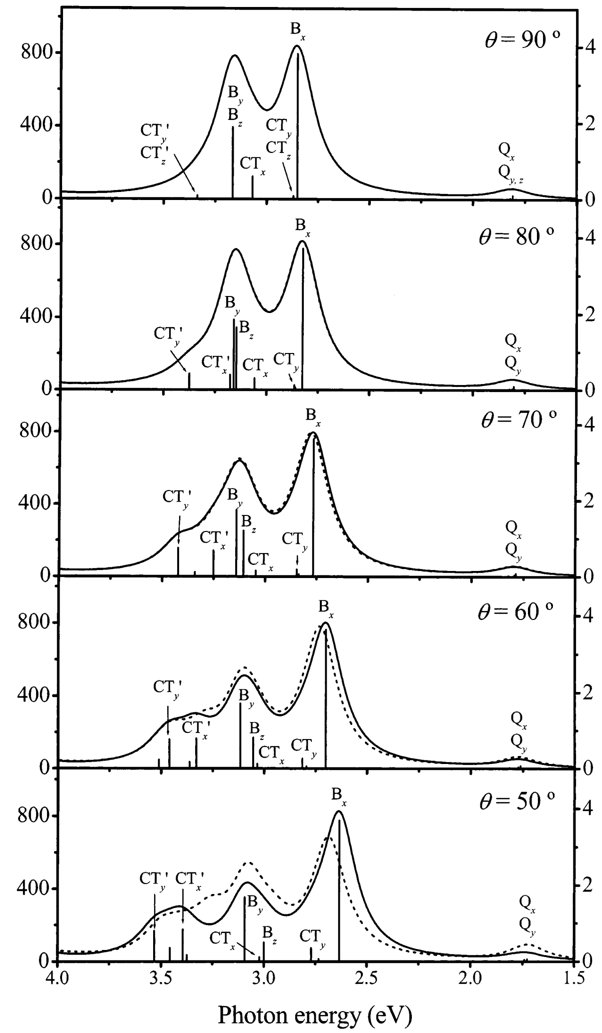

Figure 3. INDO/S−SCI simulated linear absorption spectra of diporphyrins on the basis of B3LYP optimized structures (solid line). The spectra shown by dotted lines are obtained by the dimers with undistorted porphyrin ring (i.e., the geometry optimized at $\theta = 90°$).

units, which results in a reinforcement of the coupling strength,[33,34] because the short distance between porphyrin moieties (~8.35 Å) is believed not only to enhance the through-space dipole−dipole interchromophoric electronic coupling but also to increase the through-bond interaction.

Electronic Transitions of Orthogonal Diporphyrin. The states arising from monomer's Q and B bands are designated by Q_i and B_i, respectively, where i ($= x, y, z$) stands for the orientation of the transition dipole as indicated by the present calculation ($i = 0$ for a dipole-forbidden state). We note that the degenerate B_y and B_z are close in energy to the B band of a monomer and the B_x and B_0 are split into low- and high-energy sides, respectively (Scheme 1 and $\theta = 90°$ in Figure 3). The relatively large CT (charge transfer) contribution to the B_x band, which is caused by the through-space, indirect π-conjugation, would be responsible for the overestimation of the energy separation between the B_x and B_y (B_z) bands. On the other hand, all of the Q states have more clear LE (localized exciton) character than the B states. The quite small (~0.01 eV) energy separation calculated for the Q_x and Q_y (Q_z) states leads to the assignment of the Q(0,0) band as a superimposition of these transitions and supports the vibronic nature for the shoulder (Q(2,0) band) observed on the high-energy side of the Q(1,0) band.[23]

TABLE 1: Transition Properties and Electronic Structures of the Lowest 16 Singlet Excited States of meso−meso Linked Porphyrin Dimers, as Obtained from INDO/S−SCI Calculations

state	D_{2d}	D_2	ΔE (eV)[a]	f[b]	P_{CT}(%)[c]	W_8(%)[d]
(a) $\theta = 90°$						
Q_x	B_2	B_1	1.81	0.102	2.1	96.7
Q_y	E	B_2	1.82	0.031	1.6	96.7
Q_z	E	B_3	1.82	0.031	1.6	96.7
Q_0	A_1	A_1	1.83	0	0.9	96.6
B_x	B_2	B_1	2.85	3.799	19.0	95.4
CT_y	E	B_2	2.87	0.087	92.3	93.8
CT_z	E	B_3	2.87	0.087	92.3	93.8
CT_0	A_1	A_1	3.01	0	99.1	98.5
CT_x	B_2	B_1	3.07	0.590	81.0	97.5
CT_x'	A_2	B_1	3.14	0	95.9	89.5
CT_0'	B_1	A_1	3.14	0	95.9	89.5
B_y	E	B_2	3.17	1.885	10.8	93.7
B_z	E	B_3	3.17	1.885	10.8	93.7
CT_y'	E	B_2	3.34	0.090	92.7	96.3
CT_z'	E	B_3	3.34	0.090	92.7	96.3
B_0	A_1	A_1	3.37	0	1.1	89.2
(b) $\theta = 60°$						
Q_x		B_1	1.76	0.071	5.7	96.8
Q_y		B_2	1.77	0.045	6.1	96.8
Q_z		B_3	1.81	0.024	2.6	96.7
Q_0		A_1	1.83	0	2.2	96.5
B_x		B_1	2.70	3.631	33.0	94.4
CT_z		B_3	2.80	0.063	86.0	92.7
CT_y		B_2	2.82	0.266	84.3	93.4
CT_0		A_1	2.97	0	97.2	98.1
CT_x		B_1	3.03	0.119	89.9	97.0
B_z		B_3	3.05	0.812	26.1	93.0
CT_0'		A_1	3.09	0	86.2	89.4
B_y		B_2	3.12	1.706	42.6	94.3
CT_x'		B_1	3.33	0.792	64.7	89.9
CT_z'		B_3	3.36	0.173	74.7	92.8
B_0		A_1	3.39	0	7.6	88.0
CT_y'		B_2	3.46	0.768	42.7	68.0

[a] Excitation energy. [b] Oscillator strength. [c] Interunit charge-transfer probability. [d] Total contribution of transitions within eight-orbitals to the SCI wave function.

In an energy range close to the B bands, we find eight charge-transfer (CT) states which, together with the LE (Q_i and B_i) states, form a complete set of 16 eigenstates resulting from one-electron excitations within eight orbitals (Table 1). These CT states are described as one-electron transition from the a_{1u} or a_{2u} MO of one unit to one of the e_g MOs of the other unit (refer to the Appendix 1). As can be seen from their P_{CT} values, the mixing of LE and CT character in the excited states is minimized for the orthogonal diporphyrin due to nearly prohibited π-electron delocalization between the porphyrin subunits. The energy levels of the CT states should strongly depend on the intersubunit distance (the center-to-center distance of the two porphyrins), because the Coulomb attraction between electron and hole constitutes an important stabilizing factor. In this regard, it is interesting to note that the energies of the CT_y (CT_z) and CT_x states are roughly similar to those of B_x, B_y, and B_z states, respectively ($\theta = 90°$ in Figure 3 and Table 1). This feature, which is quite specific to the meso−meso linked diporphyrin (Z2), is caused by the situation that the two porphyrins are located in a close proximity with the center-to-center distance of only 8.35 Å. In addition, the calculation has predicted that no CT state except CT_x has sufficient oscillator strength to make any significant contribution to the absorption spectrum of the orthogonal diporphyrin (Z2).

Resonance Raman Spectroscopic Measurements of Orthogonal Porphyrin Arrays. Ground-state RR spectra of Zn(II)porphyrin arrays were obtained by photoexcitation at their

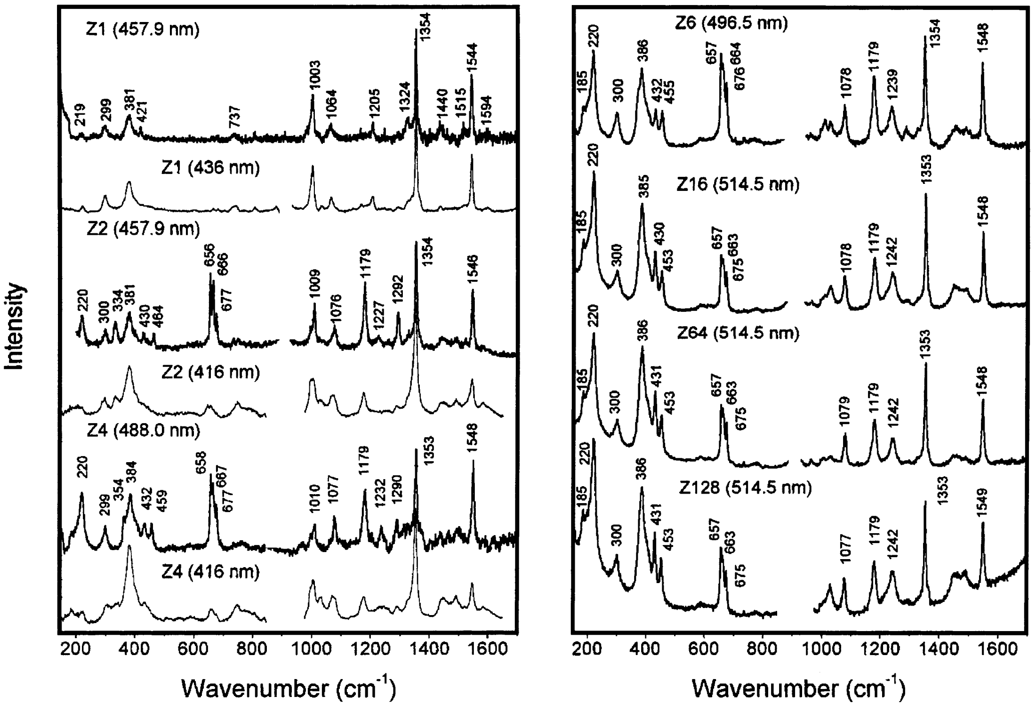

Figure 4. Series of ground-state RR spectra of the porphyrin arrays from Z1 to Z128. For Z1, the thick solid line represents the RR spectrum obtained by photoexcitation with 457.9 nm line and the thin solid line the RR spectrum by photoexcitation at 436 nm. For Z2 and Z4, the thick solid lines represent the RR spectra obtained by photoexcitation in resonance with the low-energy exciton split Soret bands and the thin solid lines are the RR spectra obtained by photoexcitation at high-energy Soret bands at 416 nm. The RR spectra for Z6, Z16, Z64, and Z128 were obtained by photoexciation in resonance with the low-energy exciton split Soret bands. Reproduced with permission from ref 22b.

low-energy exciton split Soret bands; for instance, 457.9, 488.0, and 496.5 nm for Z2, Z4, and Z6, respectively, and 514.5 nm for longer arrays, which are shown in Figure 4. The Raman spectrum of Z1 was also obtained by excitation at 457.9 nm for comparison. The Raman bands at ~1354 and ~1544 cm^{-1} in Z1, which can be assigned as the totally symmetric ν_4 and ν_2 modes, respectively, are observed at nearly the same position in each spectrum.[26] Some distinct features, however, become manifest in the Raman spectra of the porphyrin arrays. Especially, three Raman bands at ~660 cm^{-1}, where no band is observed in Z1, exhibit a systematic decrease in their intensities as the number of porphyrin units in the arrays increases. The Raman band at ~1179 cm^{-1} shows a similar trend with an increase of porphyrin units in the arrays. On the other hand, the Raman band at 220 cm^{-1} with its shoulder at 185 cm^{-1}, which is contributed by phenyl−porphyrin inter-ring stretching (195 cm^{-1} in Ni(II)TPP),[26] gains its intensity with an increase of porphyrin units in the arrays. The Raman band at 381 cm^{-1} also becomes strongly enhanced with a slight blue-shift to 386 cm^{-1} with an increase of porphyrin units. The Raman band at 1230 cm^{-1}, which is weak in Z2, gradually increases with a blue-shift to 1242 cm^{-1} with an increase of porphyrin units. The Raman bands at 1003 and 1064 cm^{-1} in Z1 are shifted to higher frequencies, and their relative intensity ratios become reverse as the number of porphyrin units in the arrays increases. These spectral features constantly appear in the RR spectra of longer porphyrin arrays, even in Z128.[35]

We have also observed the ground-state RR spectra of Zn(II) porphyrin arrays from Z1 to Z4 with excitation at their high-energy Soret bands (Figure 4).[22,36] The RR spectrum of Z1 is the same as that with 457.9 nm excitation. However, the overall Raman spectral features of Z2 and Z4 are very different from those with low-energy Soret band excitation. They closely resemble the RR spectrum of Z1, in which the new RR bands at 334, 660, and 1179 cm^{-1} are weakly observed and the RR bands at 381, 1007, 1075, 1352, and 1545 cm^{-1} that are totally symmetric modes in porphyrin monomer are predominant in the RR spectrum.[37] These observations indicate that the Raman bands of Z2 by photoexcitation at the high-energy Soret band originate predominantly from the in-plane porphyrin ring skeletal modes localized on the monomeric porphyrin ring. This is consistent with the electronic nature of the high-energy Soret band that is derived from degenerate, orthogonal, and concomitantly noninteracting B_y and B_z transitions. The similarity in the in-plane porphyrin ring skeletal modes between the constituent monomer porphyrin and Z2 indicates that the porphyrin macrocycle remains intact in its structure in the dimer.

The unique features observed in the RR spectra of the porphyrin arrays are the new Raman bands with significant intensities observed by photoexcitation at their low-energy Soret bands of which the transition dipoles lie along the long molecular axis. Through the dimerization of porphyrins combination of normal modes from each porphyrin unit gives rise to new sets of normal modes: for example, totally symmetric A_1 modes and nontotally symmetric B_2 modes are produced by symmetric and antisymmetric combination of A_g, B_{2g}, and E_u modes of porphyrin monomers, respectively, whereas additional E modes are made from E_u modes of porphyrin monomers. Interestingly these modes are not resonance activated, but only monomeric RR features are observed by photoexcitation at the high-energy Soret bands. We regard that if these kinds of Raman modes are resonance activated by a certain photoexcitation, the photoexcitation should correspond to the one that has a transition dipole along the long molecular axis. This is exactly what we observed by photoexcitation at the low-energy Soret bands of which dipoles lie along the long molecular axis. Thus, the appearance of new Raman bands is considered to reveal the

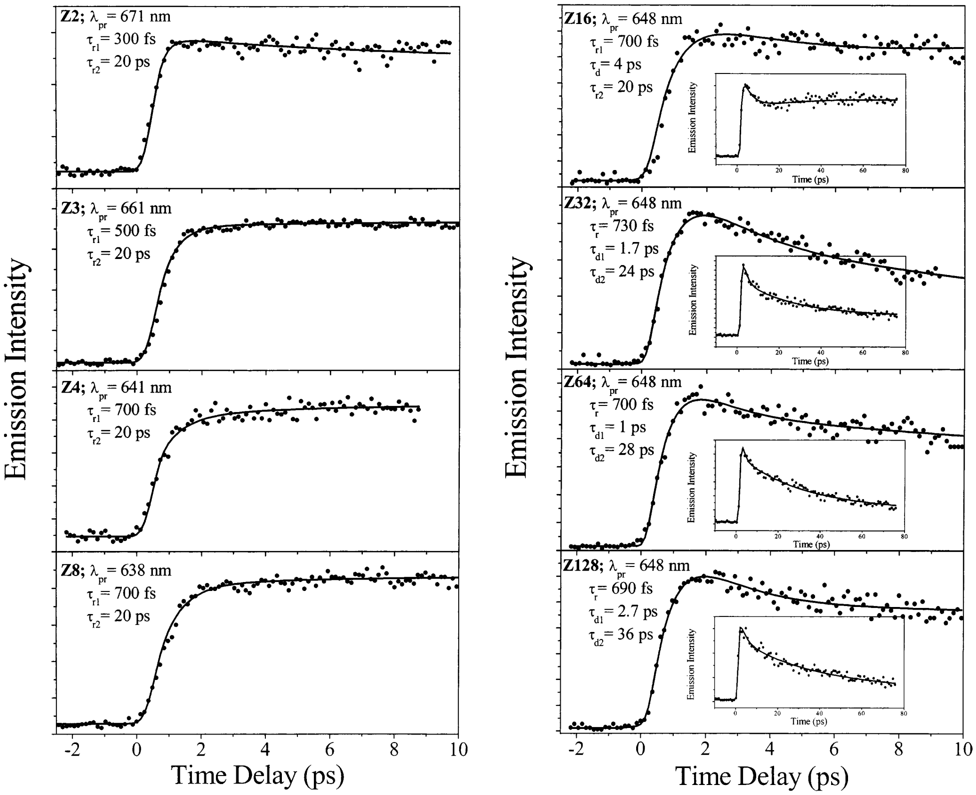

Figure 5. Fluorescence up-conversion temporal profiles of Z*n* at various probe wavelengths after photoexcitation at 400 nm. The insets show the fluorescence decay profiles up to longer delay times. τ_r and τ_d represent the rise and decay time constants, respectively. Reproduced with permission from ref 22b.

delocalized nature of the low-energy Soret bands throughout the whole porphyrin arrays.[35]

The appearance of the ~660 and 1179 cm^{-1} bands in the porphyrin oligomers suggests that these bands are associated with the bridging regions of the oligomers. We assigned the ~660 cm^{-1} bands as $C_\alpha - C_m - C_\alpha$ bending vibrations (ϕ_9, ϕ_9' and ϕ_9'') of porphyrin monomer.[26,35] The symmetric combinations of these modes with A_{1g}, B_{2g}, and E_u symmetries, respectively, give rise to three totally symmetric Raman bands with A_1 symmetry in porphyrin dimer (D_{2d} symmetry). The 1179 cm^{-1} band is attributed to the ν_{51} mode of porphyrin monomer. The ν_{51} mode itself is dominantly $C_\beta H$ bending and $C_\beta C_\beta$ stretching, but its combination mode in porphyrin dimer is found to involve the $C_m - C_m$ stretching by normal mode calculation.

One remarkable observation is the increasing relative intensities of the low-frequency Raman bands for photoexcitation wavelengths longer than 458 nm in the porphyrin arrays. One characteristic feature of Raman modes in the low-frequency region is a collective motion of atoms such that the pyrrole ring or peripheral phenyl group moves as one mass unit with almost no internal vibration. In the case of the porphyrin monomer, this feature does not seem to have significant effect on polarizability change, but when the porphyrin array length becomes longer and photoexcitation excites molecules along the long molecular axis, the collective movements of pyrrole or phenyl rings are likely to contribute accumulatively to polarizability changes in an effective manner. Thus, this feature induces the relatively large enhancement of the ν_{35} (220 cm^{-1}) and ν_8 (386 cm^{-1}) modes involving pyrrole movements and the relatively weak ϕ_{10} (300 cm^{-1}) mode involving phenyl movements.[35]

Overall, a systematic change in intensity and frequency with an increase in the number of porphyrin units clearly demonstrates that there is a strong correlation between molecular structures and Raman spectra of the porphyrin arrays. The observation that the RR spectral features of the porphyrin arrays with photoexcitation at both high- and low-energy Soret bands are different from each other indicates that the two Soret bands have distinctly different electronic nature even though they originate from the same monomeric Soret band.

Excited-State Dynamics of Orthogonal Porphyrin Arrays. The potential energy surfaces of the S_1 and S_2 states in the porphyrin monomer are almost parallel, which definitely retards the $S_2 \rightarrow S_1$ intramolecular internal conversion processes. The fluorescence temporal profile of Z1 at the red edge of fluorescence emission after photoexcitation around 400 nm exhibits the rise component with ~1.6 ps time constant, which corresponds to the $S_2 \rightarrow S_1$ internal conversion process (not shown).[38,39] Figure 5 shows the temporal profiles of the fluorescence signal in Z2, illustrating about 300 fs rise and subsequent ~20 ps decay components. The fluorescence temporal profiles of Z3 exhibit about 500 fs rise and subsequent ~20 ps rise components. As for Z4, we were able to observe a rise component with an approximately 700 fs time constant, which appeared to be a saturation value for the initial rise component with an increase in the number of porphyrin units in the arrays. The following decay component with an ~20 ps time constant was also found in the fluorescence temporal profile. In the case of Z8, a rise component with a 700 fs time constant in the fluorescence temporal profiles was observed with a subsequent rise component with an ~20 ps time constant. As for longer porphyrin arrays such as Z16, Z32, Z64, and Z128, the initial decay components with time constants of a few picoseconds are clearly seen in the fluorescence decay profiles in addition to ~700 fs rise and 20−30 ps decay components as observed in Z2−Z4 and Z8 (Figure 5).[22,40] It is to be noted that there exists a long-lived tail due to the S_1 state emission decay of the porphyrin arrays in the fluorescence temporal profiles, which should appear as a plateau in the time window (Figure 5). Thus, the time constant for this slowest decay process in the porphyrin arrays was confirmed by the TCSPC technique.

In Z*n*, the internal conversion rates are much accelerated compared with those of Z1, which could be explained by the concept of the "ladder" acting as intermediate states. The splitting of the component levels of the Soret manifold establishes a band of intermediate levels between the monomeric Soret band (B_y, B_z) and the exciton-split Soret band (B_x) in Z*n* (Scheme 1). In addition, our INDO/S−SCI calculation has revealed that the CT bands are accidentally located in the same energy. Therefore, these Soret and CT states provide a "ladder" for sequential relaxations between successive pairs of levels that are separated by energies much smaller than the S_2−S_1 energy gap in Z1.

Because the S_2' (B_x) states are the delocalized excitonic states being similar to the S_1 (Q_x) states in contrast with the monomeric localized electronic feature of the S_2 (B_y, B_z) states,[22] the electronic coupling between the S_2' and S_1 states is suggested to be stronger than that between the S_2 and S_2' states. Therefore, an excellent correlation between the S_2−S_2' energy gap and the formation time of the S_1 state suggest that the rate determining step in the overall internal conversion processes upon photoexcitation to the S_2 states in Z*n* is the $S_2 \rightarrow S_2'$ internal conversion process.

In the population dynamics of excitons in *J* aggregates, the excitation intensity dependence of the exciton lifetime observed at higher excitation densities was explained by exciton−exciton annihilation. Likewise, the initial fast decay components of 1−4 ps time constants observed in longer porphyrin arrays under the high photoexcitation density are believed to arise from exciton−exciton annihilation processes, because they exhibit the photoexcitation density dependence. The initial fast decay components become increasingly manifest in the porphyrin arrays longer than Z8 with an increase in the photoexcitation density. In the case of shorter porphyrin arrays than Z4, however, the temporal profiles remain relatively unchanged with an increase in the photoexcitation density, which suggests that two or more excitons are produced in the longer porphyrin arrays than Z4 at higher excitation densities.

The fluorescence temporal profiles for longer porphyrin arrays were obtained up to longer time delays to confirm the time constant and relative contribution of 20−30 ps rise/decay components to the overall dynamics upon photoexcitation to the S_2 states of the porphyrin arrays (insets of Figure 5). These components are believed to arise from the conversion of nonorthogonal conformers in the S_1 state to a perfectly orthogonal emitting state of the porphyrin arrays.[40] As the photoexcitation wavelength is red-shifted, these components become manifest in the temporal profiles of fluorescence signals in the porphyrin arrays because of the more preferential photoexcitation of heterogeneous conformers in the ground state at a certain wavelength (not shown). The amplitudes of these components become larger as the number of porphyrin units in the arrays increases, which suggests that the conformational heterogeneity induced by the dihedral angle distribution between the adjacent porphyrins become manifest in longer porphyrin arrays.

Coherence Length of Orthogonal Porphyrin Arrays. The coherence length has been a central issue in strongly coupled molecular aggregates or arrays and reflects a collective behavior of the transition dipole moments of pigments aligned within molecular aggregates or arrays.[41,42] With the estimated exciton coupling (V) and the homogeneous broadening (γ), we can calculate the coherence length (N_c) of porphyrin arrays. The homogeneous broadening can be estimated as follows:

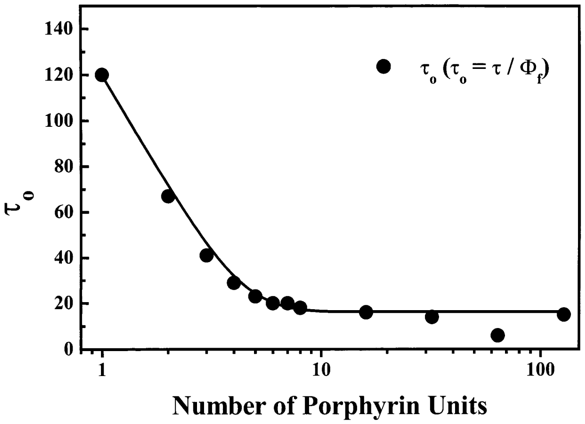

Figure 6. Plot of the number of porphyrin units in the arrays vs the relative natural radiative times obtained by the fluorescence lifetimes and the relative fluorescence quantum yields of Z*n*. Reproduced with permission from ref 22b.

$$\gamma = \frac{1}{\pi (FC)_0} = \frac{\sqrt{4\pi\lambda k_B T}}{\pi} \tag{2}$$

where λ is the reorganization energy.[22] When we consider a half of the Stokes-shift as λ, γ can be calculated to be 247 cm^{-1}.[43,44] On the other hand, by using the spectral bandwidth of the Q-band of Zn(II)TPP at 103 K,[45] γ can also be estimated to be 250 cm^{-1}. Thus, the average value of $\sim$ 250 cm^{-1} is used for γ. According to the empirical formula for the one-dimensional linear array system developed by Kakitani et al.,[46,47] the coherence length (N_c) can be estimated as follows:

$$N_c = 1.38 + 1.33 \frac{V}{\gamma} \tag{3}$$

By using this formula, the coherence length $N_c = 4.5$ for the S_1 states of Z*n* in the absence of inhomogeneity is obtained. Even when the inhomogeneous effects are incorporated (100−150 cm^{-1}), the average coherence length would be ~4.

When the pigments interact with each other and radiate in phase, the radiative decay rate becomes enhanced linearly with the number of pigment units. This radiative coherence length is defined as the ratio of the radiative decay rates with that of monomer.[48] To estimate the radiative coherence length of Z*n*, the natural radiative lifetimes are plotted in Figure 6 as a function of the number of porphyrin units in the arrays according to the relationship of $\tau_o = \tau / \Phi$ where τ_o, τ, and Φ are the natural radiative lifetime, fluorescence lifetime, and fluorescence quantum yield of Z*n*, respectively.[49,50] Because the natural radiative decay rate is expected to be proportional to the coherence length (N units) and the radiative decay rate of monomer ($k_{arrays} = Nk_{monomer}$), the crossing point value of approximately 5−6 porphyrin units seems to be a reasonable estimation of the radiative coherence length in these arrays. This radiative coherence length seems to be compatible with the estimated coherence length in the S_1 states (4.5 porphyrin units).

The electronic coupling strength and coherence length of antenna complexes in natural light harvesting system are also very important in understanding the energy transfer efficiency and the related excitation energy flow. For example, the Bchl *a* molecules of B850 ring in LH2 are strongly coupled with each other and the elementary excitation is delocalized over several pigments, not localized on the monomer. This excitonic

CHART 2

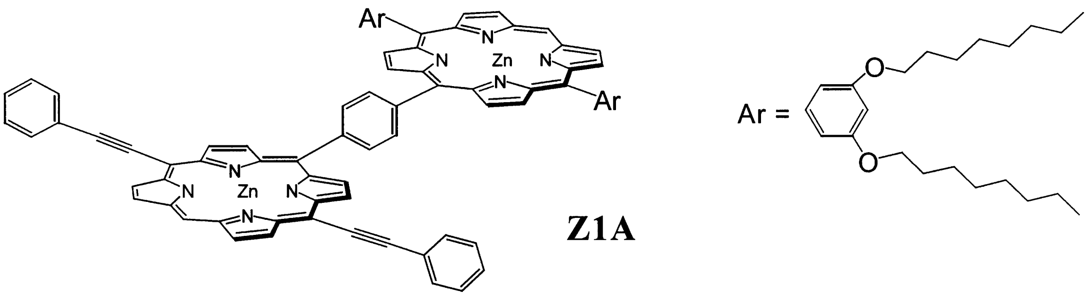

Z1A

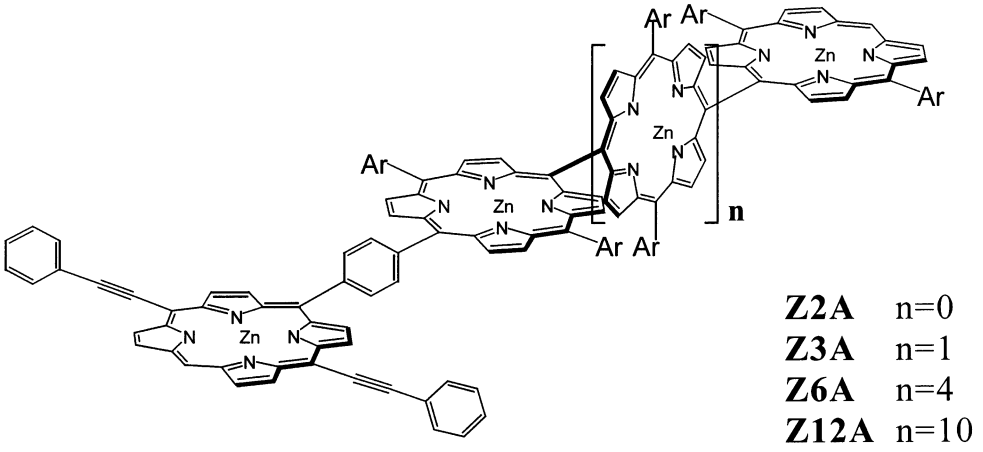

Z2A n=0
Z3A n=1
Z6A n=4
Z12A n=10
Z24A n=22

delocalization in the light harvesting system is determined from the inter-pigment coupling strength (constructive factor) and the line broadening effect such as electron−phonon coupling and site inhomogeneity (destructive factor).[46] Numerous theoretical and experimental methods have been utilized to assess the size of exciton delocalization in LH2. From these studies, it has been demonstrated that the coherence length of the strongly coupled B850 ring in LH2 is about 4 Bchl *a* molecules.[48,51,52] Because the coherence length of Z*n* is compatible with that of B850 in natural light harvesting system, our porphyrin array systems suggest to be promising in the framework of mimicking natural light harvesting arrays.

Highly Efficient Energy Transfer System Based on Orthogonal Porphyrin Arrays. Directly linked porphyrin arrays (Z*n*) as the energy donor are expected to realize fast and highly efficient energy transfer owing to the repeated regular arrangement of porphyrin rings with large electronic interactions. We have investigated the energy transfer processes of donor−acceptor systems as shown in Chart 2 (Z*n*A; $n = 1, 2, 3, 6, 12,$ and 24) in which the *meso*−*meso*′-bisphenylethynylated porphyrin acceptor is linked to an end meso carbon of Z*n*.

The absorption spectra of hybrid porphyrin arrays in the Q-band region are essentially given by the sum of the absorption spectra of meso−meso linked porphyrin arrays (Z*n*) and energy acceptor moiety (A), indicating that electronic interactions in the ground state are relatively weak, whereas Soret bands are considerably affected owing to their large transition dipole moments to yield red-shifted and exciton split absorption spectra (Figure 7, parts a and c). This feature enables a selective photoexcitation of the donor to track down the energy flow from the photoexcited donor to the acceptor. In addition, the donor emission and the acceptor absorption are very well overlapped with each other, being favorable for the rapid energy transfer. As shown in the insets of Figure 7, parts a and c, the fluorescence emission of Z*n*A comes only from the acceptor moiety, bisphenylethynyl substituted porphyrin, being indicative of facile energy transfer.

A series of transient absorption spectra of Z1A−Z24A were obtained by selective photoexcitation of Z*n*, which revealed that the energy transfer process from photoexcited Z*n* to acceptor component A occurs very fast and quantitatively. The kinetic profiles for transient absorption spectral changes for Z1A−Z24A represent the energy transfer process. The excitation energy transfer (EET) rates could be estimated from the ground-state bleaching recovery of donor moieties and the stimulated emission of acceptor unit, of which photoexcitation and detection wavelengths are indicated in Figure 7, parts b and d for Z1A and Z6A as representative examples of Z*n*A systems. The EET rate constants were determined to be $(2.5\ \text{ps})^{-1}$ for Z1A, $(3.3\ \text{ps})^{-1}$ for Z2A, $(5.5\ \text{ps})^{-1}$ for Z3A, $(21\ \text{ps})^{-1}$ for Z6A, $(63\ \text{ps})^{-1}$ for Z12A, and $(108\ \text{ps})^{-1}$ for Z24A.

To describe the energy transfer dynamics in Z*n*A, we have employed three theoretical models, that is, Förster mechanism, energy hopping, and a simple quantum-mechanical model. First, the EET between donor and acceptor is approximately explained by point dipole−dipole interactions, the so-called Förster mechanism,[53,54] assuming that the donor array was considered as one single chromophore in this model, resulting in

$$k = \frac{8.8 \times 10^{-25} \kappa^2 \Phi J}{n^4 R^6 \tau} \tag{4}$$

$$J = \int F(\nu)\epsilon(\nu)\nu^{-4}\, d\nu \tag{5}$$

where n is the refractive index of the solvent, R is the center-to-center distance between donor and acceptor, Φ is the fluorescence quantum yield of donor, τ is the fluorescence lifetime of donor, κ is the dipole−dipole orientation factor, and J is the spectral overlap integral. On the basis of eqs 4 and 5,

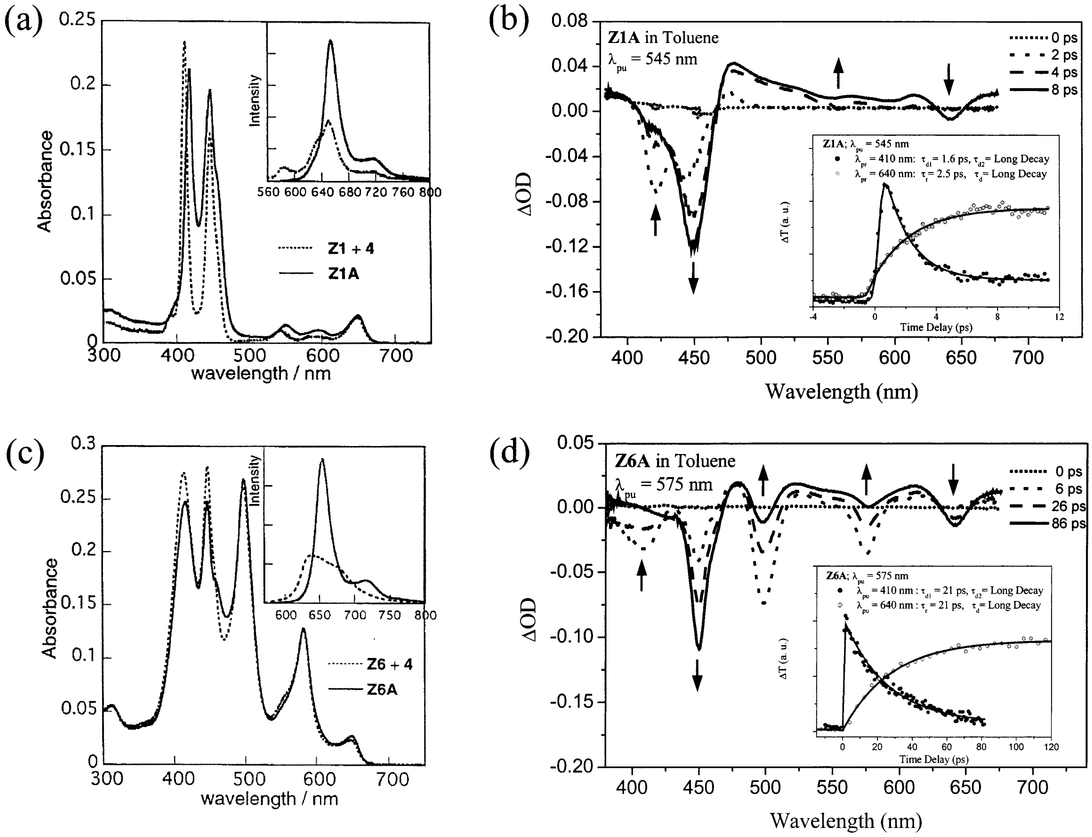

Figure 7. Absorption spectra and transient absorption spectra of Z1A for (a), (b) and Z6A for (c), (d). The emission spectra of each donor–acceptor and 1:1 mixed system after selective photoexcitation of energy donors are shown in the insets of (a) and (c). The bleaching recovery and stimulated emission temporal profile of donor and acceptor are shown in the insets of (b) and (d).

the Förster energy transfer rate constants are estimated to be (5.2 ps)$^{-1}$ for Z1A, (6.9 ps)$^{-1}$ for Z2A, (20 ps)$^{-1}$ for Z3A, (160 ps)$^{-1}$ for Z6A, (2300 ps)$^{-1}$ for Z12A, and (49000 ps)$^{-1}$ for Z24A. These slow energy transfer rates stem from the intermolecular distance (R) term, which means that the meso–meso linked porphyrin array cannot be assumed as one chromophore and the through-bond contribution via phenylene linkage to the overall energy transfer from Zn to A will be significant. Thus, the following two mechanisms are considered.

We considered each porphyrin moiety in Zn as one chromophore. The energy hopping in the donor arrays may be one of considerable mechanisms. In this calculation, we employed a matrix-formulated eigenvalue/eigenvector approach implemented by Donohoe and co-workers,[55] using empirical data to predict the quantum efficiency. In our case, assuming that the absorption characteristics of each porphyrin unit in the donor are identical, the energy transfer scheme was given as follows:

$$\mathrm{Z}n{-}\bullet\bullet\bullet{-}\mathrm{Z2^*{-}Z1{-}A} \underset{k_{-1}}{\overset{k_1}{\longleftrightarrow}} \mathrm{Z}n{-}\bullet\bullet\bullet{-}\mathrm{Z2{-}Z1^*{-}A} \xrightarrow{k_2} \mathrm{Z}n{-}\bullet\bullet\bullet{-}\mathrm{Z2{-}Z1{-}A^*}$$

The model yields pseudo-first-order rate because k_1 would be much faster than k_2, which is predictable from the fact that the excitation energy hopping rate in Zn is estimated to be (~0.2 ps)$^{-1}$ in the previous femtosecond transient absorption anisotropy decay of Zn and the energy transfer rate from photoexcited Zn(II) porphyrin to free-base porphyrin in the meso–meso phenylene linked porphyrin heterodimer was evaluated to be (~3 ps)$^{-1}$.[22] Thus, we can obtain the following equation:

$$\frac{\mathrm{d}A^*}{\mathrm{d}t} = k_2 \mathrm{Z1}^* \approx \frac{k_2}{n} \qquad (6)$$

TABLE 2: Fluorescence Data and Observed and Calculated EET Rate Constants

model	R(Å)[a]	k_{obs} (ps^{-1})[b]	k_{EN} (ps^{-1})[c]	k_{EN} (ps^{-1})[d]	k_{EN} (ps^{-1})[e]
Z1A	12.7	2.5 ± 0.1	5.2		
Z2A	16.9	3.3 ± 0.2	6.9	5.0	3.4
Z3A	21.0	5.5 ± 0.5	20	7.5	4.7
Z6A	33.6	21 ± 2	160	15	23
Z12A	58.6	63 ± 5	2300	30	70
Z24A	109	108 ± 7	49000	60	163

[a] Center to center distances between the donor and the acceptor. [b] EET rate constants measured by the transition absorption spectra. [c] EET rate constants calculated from eq 4. [d] EET rate constants calculated from eq 6. [e] EET rate constants calculated from eq 8 when $L = 4$.

where A* and Z1* represent the local excited state of A and Z1, respectively. The values calculated from eq 6 are shown in Table 2, which does not seem to be so outrageous, though they still show some deviations from the values observed by transient absorption method.

Finally, we would like to consider the energy transfer rate from simple quantum mechanical treatments. In our well-defined array system, the energy transfer rate (k_N) can be expressed by using the time-dependent perturbation theory (refer to the Appendix 2 for the details)

$$k_N \approx \frac{2}{N+1}\left[\sum_{n=1}^{N}\left(\frac{R_1}{R_n}\right)^3 \sin\left(\frac{\pi}{N+1}n\right)\right]^2 k_1 \qquad (7)$$

where N is the number of porphyrin units in the donor array and R_n represents the distance between the nth donor and acceptor.

Equation 7 was obtained with the assumption that the lowest exciton state is coherently coupled with all molecules in the

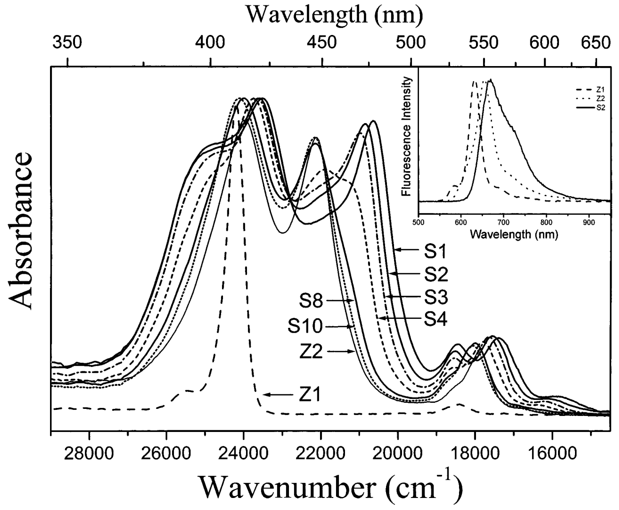

Figure 8. Absorption spectra of Z1, Z2, and S*n* in toluene. Inset shows the fluorescence spectra of Z1, Z2, and S2 in toluene after photoexcitation at 400 nm. Reproduced with permission from ref 23d.

donor aggregates, which is acceptable when N is small. When N is large, however, the lowest exciton state should be coherently coupled by only a limited number L, because the coherence is easily disrupted at long distance. In this case, the lowest exciton states exist by a number of $N - L + 1$ on the linear array. Let us assume, for simplicity, that the lowest exciton states are realized with the same probability of $1/(N - L + 1)$, where eq 7 should be replaced by

$$k_N = k_L/(N - L + 1), \quad \text{when } N > L \tag{8}$$

The EET rate constant relative to that of **Z1A** ($N = 1$) is given by k_1/k_N. When L was set variable, the most reliable rate constant was calculated for $L = 4$, and the calculated EET rate constants are listed in Table 2. We see therein that the calculated results are in a good agreement with the observed ones. Therefore, this quantum mechanical theory seems to be most suitable, again supporting a view that the excited states of the tightly bound porphyrin arrays should be excitons covering a number of molecules coherently. Equation 6 corresponds to a special case of eq 8 for $L = 1$. Conclusively, all donor−acceptor systems (Z*n*A) illustrate highly efficient molecular photonic wire due to large excitonic interactions in Z*n* arising from a close proximity and a lack of energy sink owing to well-defined orthogonal geometry along the arrays.

IV. Photophysical Properties of Strapped Diporphyrins: S*n*

Steady-State Absorption Spectra of Strapped Diporphyrins. Figure 8 shows the absorption spectra of Z1, Z2, and S*n* in toluene, indicating that the spectra of S*n* are more complicated than those of Z1 and Z2. The dihedral angle between the two porphyrins in S*n* decreases by shortening a strap chain length (Scheme 1), which is followed by structural distortions and drastic absorption spectral changes. In going from S10 to S1, the absorption spectra exhibit systematic changes both in the B- and Q-band regions, whereas S10 exhibits similar split Soret bands at 414 and 447 nm to those of Z2 except a slight broadening. The intensities of the split Soret bands around 415 and 450 nm decrease, and the absorption bands around 400 and >460 nm are intensified, particularly in S3, S2, and S1. In S2, the monomeric band at 412 nm is split into two bands at 397 and 424 nm, which indicates that there exist $B_y \pm B_z$ pair interactions between the parallel transition dipoles such as the case of H aggregates.[31] The strong interactions along the intermolecular axis give rise to the absorption band at 478 nm, whereas the higher energy split band is not allowed due to out-of-phase interference of transition dipoles. In the absorption spectrum of the most planar S1, three distinct bands are observed at 395, 425, and 483 nm in the Soret band region. In S*n*, the exciton coupling framework suggests that the dipole-allowed $B_x + B_x$ states should appear at the same position for all of the strapped diporphyrins, because the Coulombic interaction in $B_x + B_x$ should be independent of the dihedral angle. However, the exciton split B band of S1 is further red-shifted from 450 to 483 nm, which indicates that the cumulenic resonance interaction should be considered to be responsible for the red-shift of the split B band. Along with these changes, the Q bands display systematic changes including a change from a prominent Q(1,0) band at 552 nm and a weak Q(0,0) band at 589 nm in S10 to distinct Q(2,0) and Q(1,0) bands at 540 and 572 nm, and a weak Q(0,0) band at 625 nm in S1.

The structures of S*n* estimated by MM2 calculations indicate that the porphyrin rings in S10 and S8 are almost flat with negligible mean plane deviations and arranged roughly in a perpendicular manner with the dihedral angles of 94° and 89°, respectively, along the meso−meso linkage. For S*n* with shorter straps, the dihedral angles have been calculated as follows: 79° (S6), 75° (S5), 70° (S4), 47° (S3), 41° (S2), and 36° (S1). The X-ray data of Cu(II) complexes of Z2, S2, S4, and S8 analogues have also provided very useful structural information on their corresponding Zn(II) porphyrin dimers.[23] It was revealed that Z2 (Cu) is composed of two quite planar porphyrin rings (the mean plane deviation of porphyrin ring; $\varphi = 0.05$ Å) by orthogonal conformation. On the other hand, a single structure of S8 (Cu) exhibiting two ruffled porphyrin rings ($\varphi = 0.33$ and 0.35 Å) connected by meso−meso bond length of $\chi = 1.50$ Å with the dihedral angles of $\theta_1 = 64.9°$ and $\theta_2 = 80°$ (θ_1 and θ_2 are the dihedral angles between porphyrins at strapped and unstrapped sides, respectively) was observed. In S2 (Cu) and S4 (Cu), two different conformers (A and B) packed in a pairwise manner were observed. In the crystal of S2 (Cu), the A structure exhibits $\varphi = 0.46$ and 1.30 Å, $\theta_1 = 50.6°$, $\theta_2 = 59.4°$, and $\chi = 1.52$ Å and the B structure exhibits $\varphi = 0.15$ and 1.64 Å, $\theta_1 = 50.3°$, $\theta_2 = 55.0°$, and $\chi = 1.48$ Å. Similarly, in S4 (Cu), the A structure exhibits $\varphi = 0.65$ and 0.72 Å, $\theta_1 = 60.8°$, $\theta_2 = 67.5°$, and $\chi = 1.53$ Å and the B structure exhibits $\varphi = 0.61$ and 0.70 Å, $\theta_1 = 53.2°$, $\theta_2 = 58.8°$, and $\chi = 1.47$ Å. A and B conformers have nearly the same mean plane deviations but differ largely in the meso−meso bond length, which is longer in A and shorter in B.

The inset of Figure 8 shows the steady-state fluorescence spectrum of S2 in toluene as well as those of Z1 and Z2. It is worth noting that S2 exhibits a broad fluorescence spectrum extended to NIR region with a large red-shift (~1000 cm^{-1}), whereas the spectral bandwidth of Z2 is similar to that of Z1 with a little red-shift (~500 cm^{-1}). The fluorescence spectrum of S2 also reveals a shoulder at 725 nm in addition to the main band at 670 nm. The two isomers are expected to have different photophysical properties, because the conformers have different interporphyrin distances, i.e., the B conformer with a shorter interporphyrin distance is expected to have stronger intermolecular interactions than the A conformer. These results suggest that there exist at least two emissive isomers having different photophysical properties in S2.

Molecular Orbital (MO) Considerations. To understand the absorption spectra of the strapped diporphyrins, we started with a simple quantum chemistry consideration[56,57] and proceeded to more sophisticated calculations as described in the following. Initially, the strapped diporphyrins are modeled as porphyrin dimers with variable dihedral angles (θ) between the meso−meso linkage as displayed in Scheme 1. All of the geometries were optimized by using the B3LYP hybrid density-functional theory as implemented in the Gaussian 98 suite.[28] The structures of monomer and orthogonal diporphyrin were fully optimized under D_{4h} and D_{2d} symmetrical constraints, respectively, and have been calculated to gain the minimum energy structures by performing the normal-mode analysis. For the diporphyrins with $\theta < 90°$, all of the geometrical parameters except θ were optimized assuming D_2 symmetry. The energy minimum is rather shallow around 90°, but the B3LYP total energy starts to increase significantly at around $\theta = 60°$ presumably because of the increasing steric repulsion between the peripheral β hydrogens adjacent to the meso−meso linkage. It is noteworthy that this repulsion also induces significant distortion in the porphyrin planes.

The absorption spectra of the model diporphyrins were calculated by the single excited configuration interaction (SCI) method on the basis of the intermediate neglect of the differential overlap model for spectroscopy (INDO/S) Hamiltonian.[58] On the basis of SCI, the absorption spectrum was calculated by the standard sum-over-states formula[59] assuming a lifetime broadening of 0.1 eV for all of the excited states. The energy levels of the frontier eight orbitals for the diporphyrins obtained from INDO/S calculations are formed by combinations of monomer's four frontier orbitals.[60] The INDO/S−SCI simulated absorption spectra for the dimers of $\theta < 90°$ are previously displayed in Figure 3 (solid lines) and the transition properties of the lowest 16 excited states for the diporphyrin with $\theta = 60°$ are listed in Table 1, which shows that experimentally observed features are well reproduced. To reveal the influence of ring distortion, we have also performed INDO/S−SCI calculations for the dimers composed of flat porphyrin subunits whose geometries were obtained by changing only θ in the optimized geometry of the orthogonal dimer. The results are plotted by the dotted lines in Figure 3. We note that the spectral changes are caused essentially by the dihedral angle, whereas the ring distortion enhances the absorption on the high-energy side of the B_y band. The symmetry lowering from D_{2d} to D_2 lifts the degeneracy of the excited states, where the splitting of the B_y−B_z pair follows the exciton coupling scheme with the B_y carrying more intensity and lying at the high-energy side. However, their energy separation is so small (0.07 eV at $\theta = 60°$) that they would merge into a single band that probably corresponds to an intense peak around 420 nm in the S3, S2, and S1 spectra. On the other hand, as shown in Figure 3, we find that the absorption appearing on the high-energy side of the B_y band (about 400 nm in the S3, S2, and S1 spectra) is formed by a superposition of the CT'_x and CT'_y transitions. As shown in Table 1, these states show remarkable enhancement in their oscillator strengths and the CT'_x is significantly blue-shifted at $\theta = 60°$ relative to the case of $\theta = 90°$. In this regard, it is worthwhile to point out that the ring distortion enhances the blue-shift of the CT'_x; this may be responsible for the more pronounced peak calculated for the ring-distorted geometry.

In the energy region between the B_x and B_y bands, we note that the oscillator strength of the CT_y state is significantly enhanced, whereas that of the CT_x state is attenuated with a decrease in the dihedral angle. In addition, the associated red-shifts of these CT states are less prominent relative to that of the B_x band. The above-mentioned intensification of the CT_y, CT'_x, and CT'_y states can be ascribed to the enhanced LE character in their electronic structures when $\theta = 60°$ (Table 1). Moreover, this situation can be regarded as a result of configuration mixing between these CT states and B_i ($i = x, y$) states caused by the increased meso−meso π conjugation.

In contrast to the case of the B_y−B_z pair, the calculation predicts that the Q_y shifts to the low-energy side of the Q_z as θ deviates from 90°. Thus, the red-shifted Q(0,0) band observed for S*n* would be assigned to a superposition of the Q_x and Q_y transitions. Note that, in contrast to the B states, all of the Q states retain their LE character, even for the twisted geometries because of their energy separation from the CT states that prohibits efficient configuration interactions among them. This calculation has shown that the red-shifts of the Q_x (Q_y), B_x, and B_y bands, in going from $\theta = 90°$ to 60°, are 0.05 (0.05), 0.15, and 0.05 eV, respectively, which are in a good agreement with the corresponding values of 0.12, 0.18, and 0.08 eV obtained from the S10 and S2 spectra.

As discussed above, the INDO/S−SCI calculation has successfully predicted the significant contribution of several CT states (especially the CT'_x and CT'_y) to the spectral changes caused by the shortening of the strap length in S*n*, which are accidentally located in energy close to the excitonic transitions, including the B_x, B_y, and B_z bands. Because the simple exciton coupling theory is insufficient to explain the photophysical properties of S*n*, the INDO/S calculation is quite complementary, successfully addressing the unique photophysical properties of S*n*.

Resonance Raman Spectra of Strapped Diporphyrins. A series of RR spectra of S*n* by photoexcitation at 457.9 and 488.0 nm are shown in Figure 9 together with the RR spectrum of Z2 for comparison. They show quite different RR enhancement pattern depending on the photoexcitation wavelength, which is attributable to the electronic nature of the relevant absorption band. The RR spectra of S*n* by photoexcitation at 488.0 nm exhibit nearly the identical RR enhancement pattern except a large enhancement of the low-frequency modes below 500 cm^{-1} in going from S10 to S1. Most of the Raman bands are attributed to the totally symmetric modes spanning the A_1 symmetry under the D_{2d} point group of Z2 like the Raman bands of S10 by photoexcitation at 457.9 nm. The Raman bands at 1545, 1352, 1291, 1184, 1005, and 386 cm^{-1} in the RR spectrum of S10 are attributed to the ν_2, ν_4, ν_{27}, ν_{51}, ν_6, and ν_8 modes of the porphyrin monomer.[23c] The large enhancement of the triple bands at around 666 cm^{-1} that originate from $C_\alpha C_m C_\alpha$ bending vibration is also observed. These typical features are observed from S10 to S1 by 488.0 nm excitation, revealing a consistency with the MO calculation that the absorption band of S1 at 478 nm possesses the excitonic nature polarized along the long molecular axis.[23c]

The RR spectrum of S10 by photoexcitation at 457.9 nm is nearly the same as that of Z2, exhibiting the dominant enhancement of the totally symmetric A_1 modes under the D_{2d} symmetry point group of Z2. In going from S10 to S1, however, the RR enhancement pattern shows systematic changes. The Raman bands at 1519, 1490, 1444, and 1023 cm^{-1} become gradually stronger, and the low-frequency bands such as the ν_8 mode at 387 cm^{-1} lose their intensities. The gradual enhancement of these RR bands in going from S10 to S1 indicates that the electronic nature of the corresponding transition is quite different from the red-shifted excitonic band at around 480 nm. The spectral changes can be understood comparatively by the electronic property changes that the position of the low-energy exciton transition ($B_x + B_x$) is shifted from 450 to 480 nm with

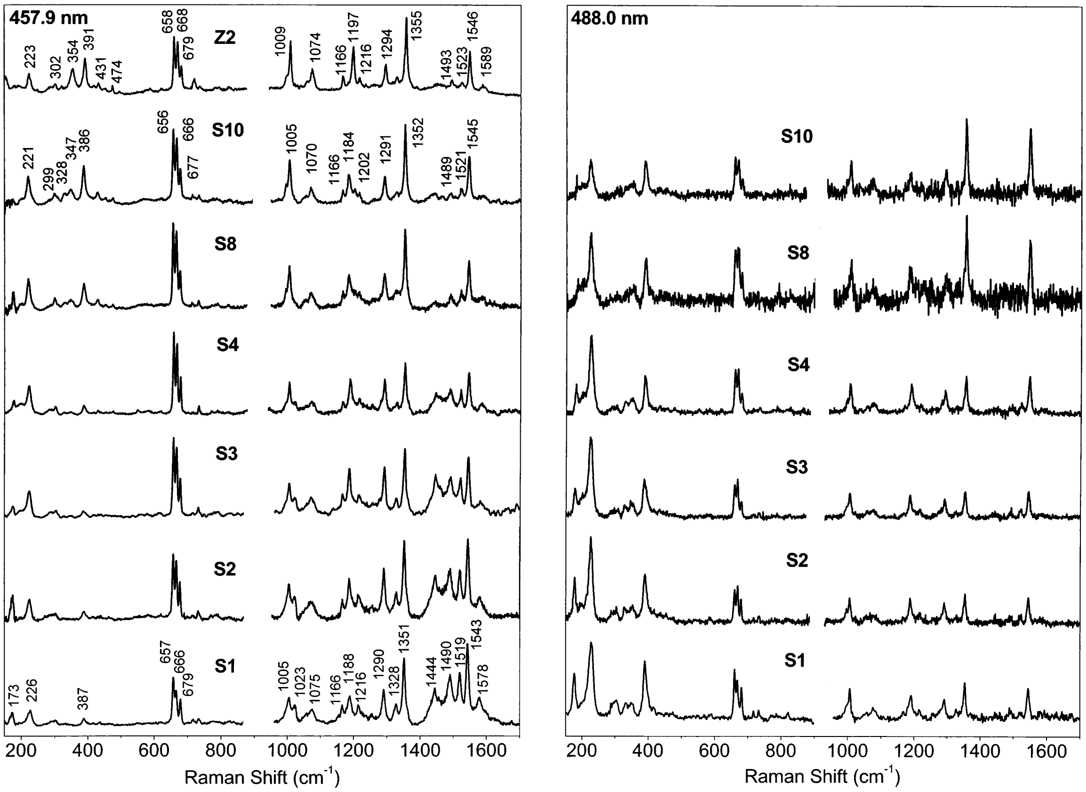

Figure 9. Resonance Raman spectra of Z2 and S*n* in THF by excitation at 457.9 nm (left column) and those of S*n* by excitation at 488.0 nm (right column). Reproduced with permission from ref 23c.

a decrease of the strap length, whereas a new CT_y transition appears around 450 nm with considerable intensity. As the low-energy exciton band is shifted out of the CT_y band, the RR enhancement of excitonic nature becomes reduced and that of CT nature becomes manifest. The new spectral features observed in S*n* with a short strap length by 457.9 nm excitation are analyzed in terms of the B-term scattering between the relevant CT transition and nearby strong excitonic transitions.[23c] The transition density matrix calculation revealed that C_α and C_β atoms have large spatial overlap, which explains successfully the observed RR bands, for instance, appearing at 1519, 1490, and 1444 cm^{-1}. They are assigned as the ν_{38}, ν_{11}, and ν_3 modes, respectively. All of them involve large movement of $\nu(C_\alpha C_\beta)$ and/or $\nu(C_\beta C_\beta)$ vibrations.[23c] However, we cannot totally neglect the contribution from the A-term scattering from the CT_y transition itself considering its considerable, even if relatively weak, oscillator strength and mixed nature between CT and excitonic characters observed in the MO calculation.[23c]

The RR spectra of Sn obtained by photoexcitation at 406.7 nm are nearly the same irrespective of the dihedral angle change (not shown).[23c] The RR spectra exhibit spectral features characteristic of the porphyrin monomer, indicating that the high-energy Soret bands of S*n* largely maintain monomeric character in going from S10 to S1. This supports the MO calculation showing that the B_y and B_z transitions are still nearly independent and have substantially monomeric characters.[23c]

Excited-State Dynamics of Strapped Diporphyrins. The fluorescence decay profiles of S*n* show similar temporal profiles with single-exponential decay, indicating that the lifetimes of the lowest excited singlet states of S*n* are quite similar despite their structural distortions such as mean plane deviations and existence of two conformers. However, although the time constant of S10 (1.96 ns) is comparable to the fluorescence lifetime (1.98 ns) of Z2, the time constant gradually decreases, i.e., 1.84, 1.82, 1.77, 1.65, and 1.53 ns for S8, S4, S3, S2, and S1, respectively. Judging from the X-ray data and MM2 calculations of S*n*, we can find a trend that the mean plane deviations become gradually severe in going from S10 to S1. In this regard, a systematic decrease in the overall fluorescence lifetimes suggests that the porphyrin ring distortions of S*n* have a good correlation with the overall fluorescence lifetimes as compared with Z2 having planar porphyrin rings. In S*n*, charge-transfer states are accidentally located in the energy region spanned by the split Soret bands. However, no charge-transfer or charge-resonance transitions but only Q bands exist in near S_1 region, which explains why the lowest excited-state decay of S*n* is not affected much by a change in the dihedral angle as well as the interporphyrin distance.

To explore the conformational dynamics, if any, possibly occurring in much faster time scale, S2 is suggested to be a representative candidate having small dihedral angle with mean plane deviation and two conformers, because S1 becomes disintegrated slowly under prolonged laser light illumination and the conformational effect induced by reduced dihedral angle is suspected to be not so large in S4. To investigate the relaxation dynamics of S2 occurring in a faster time domain, we carried out femtosecond fluorescence upconversion experiment. Figure 10 shows the temporal profiles at the two different probe wavelengths of 562 and 668 nm. The global deconvolution at 562 nm gave the two time constants of ~0.5 and 15 ps as decay and rise components, respectively, whereas the two time constants of ~0.5 and 15 ps were obtained at 668 nm as rise components. As shown in the inset, the time constant of 1.65 ns was also observed in much slower time interval at 668 nm.

Figure 11 displays the transient absorption spectra of Z1, S2, and Z2 in toluene upon photoexcitation at 400 nm at various time delays. In the NIR region from 700 to 1000 nm, no typical spectral structures have been observed for both Z1 and Z2 within

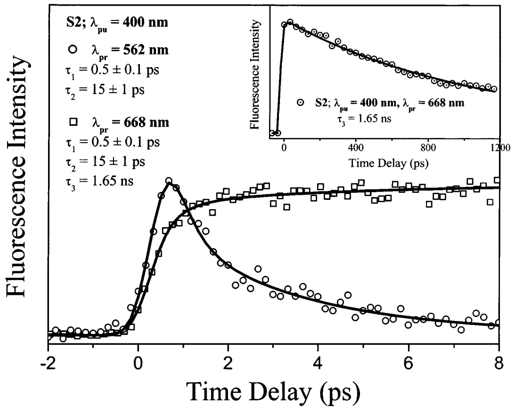

Figure 10. Fluorescence temporal profiles of S2 at 562 and 668 nm after photoexcitation at 400 nm, which were obtained by fluorescence upconversion technique. The inset shows the fluorescence temporal profile at 668 nm with the time constant of 1.65 ns in longer time window after photoexcitation at 400 nm. Reproduced with permission from ref 23d.

a delay time of a few hundred picoseconds. On the other hand, S2 exhibits a broad band structure of the stimulated emission at around 650 nm, of which the bandwidth is about four times broader than those of Z1 and Z2, which is consistent with the steady-state fluorescence spectra shown in the inset of Figure 8. The decay profiles of S2 were observed at 480, 660, and 900 nm after photoexcitation at 400 nm, which correspond to the ground-state bleaching, stimulated emission, and photoinduced absorption, respectively (the right side column of Figure 11). The stimulated emission decays with the two different time constants of 0.5 and 15 ps, which are similar to those observed in the fluorescence upconversion experiment (Figure 10). A rise component was also observed with the time constant of 0.5 ps at 900 nm, which is attributed to the $S_2 \rightarrow S_1$ internal conversion process. Following fast energy relaxation dynamics with the time constant of 0.5 ps, the lowest excited state relaxes slowly with the time constant of 1.65 ns. The 0.5 ps time constant of S2 is a little slower than that of Z2 (0.3 ps), which is consistent with a trend that the internal conversion to the lowest excited-state becomes slower as the exciton split Soret band is more red-shifted, because the energy difference between the monomeric Soret band and the split Soret band increases.[22]

On the other hand, following fast energy relaxation dynamics with the time constant of 0.5 ps, the 15 ps component was also observed in the fluorescence upconversion and stimulated emission decay profiles. A careful inspection shows that the component with the time constant of 15 ps increases in the ground state bleaching signals, as the probe wavelength decreases from 480 to 420 nm after photoexcitation at 395 nm, which is generally opposite to the vibrational cooling process.[61,62] The photoinduced absorption signal was observed to have a broad spectral feature in this probe region (Figure 11), indicating that the dynamics in the excited states can be mixed with the ground-state bleaching signal. In addition, the components with the time constant of 15 ps in the ground state bleaching signals at the same probe wavelength, i.e., 420, 445, and 480 nm, were reduced slightly when the pump wavelength was changed from 395 to 400 nm. Thus, we suggest that the time constant of 15 ps originates from the decay dynamics of the photoinduced absorption, which leads to the conclusion that the conformational dynamics is the most probable arguments.

We note that the conformational dynamics of S2 (∼15 ps) is a little faster than that of Z2 (∼20 ps). The existence of two conformers in S2 is largely responsible for the fast conformational dynamics, whereas it is also suggested that the activation barrier for the conformational dymanics in S2 is lower on reaction coordinate.[22,23] After the Soret band photoexcitation, Z2 in the excited state in the Franck−Condon region proceeds to reach an equilibrium position on the excited potential energy surface, where the probable reaction coordinate could be ascribed to the dihedral angle between the porphyrin macrocycles. Unfortunately, however, it is difficult to assign the reaction coordinate in S2 clearly because of the expectedly complicate structural changes.

V. Photophysical Properties of Fused Porphyrin Arrays: T*n*

Steady-State Absorption Spectra of Fused Porphyrin Arrays. Figure 12 shows the absorption spectra of the fused Zn(II) porphyrin arrays (T*n*) in $CHCl_3$. The fused porphyrin arrays display drastically red-shifted, even to the IR region, absorption spectra reflecting extensive π-electron delocalization over the array. The absorption bands of the fused porphyrin arrays are roughly categorized into three distinct well-separated bands, which are marked as B_y, B_x, and Q_x bands in near UV, visible, and IR regions, respectively, on the basis of their transition properties revealed by the PPP−SCI calculations.[25] The bands in the near UV region retain nearly the same positions as that of the Zn(II) porphyrin monomer, but a significant broadening in their bandwidths occurs. In contrast, the absorption bands in the visible and IR regions continuously shift to the red as the number of porphyrin units increases. Along with a continuous red-shift in the absorption bands of longer arrays, the relative intensities of the B_x and Q_x bands are increasingly stronger as compared with the B_y bands. It is also noteworthy that the absorption in the interval wavelength regions between three distinct absorption bands becomes enhanced upon elongation of the fused porphyrin arrays, which implies that more complicated and congested electronic states lie in energy regions between three main bands of longer fused Zn(II) porphyrin arrays.

Molecular Orbital (MO) Considerations. The frontier orbital energy levels of the Zn(II) tetraphenylporphyrin monomer (Zn^{II}TPP) and T2 are shown in Figure 13a as obtained by the INDO/S−SCI calculations. As indicated in Figure 13a, the highest four occupied and the lowest four unoccupied orbitals of **T2** are formed by the combinations of the monomer's "four orbitals"[60] with their significant energy splittings relative to the monomer levels. Because the orbital pattern of these eight orbitals is essentially the same as that obtained by the previous PPP calculation,[25] only the HOMO and LUMO among them are depicted in Figure 13a. It is noteworthy that the LUMO of T2 exhibits significant bonding amplitudes at all of the three linkages (meso−meso and two $\beta_1-\beta_1'$), whereas the antibonding contribution is essentially restricted to the meso−meso linkage for the HOMO in consistent with the much larger energy-shift of the former than that of the latter. Therefore, the progressive red-shift of the Q_x band of T*n* would be largely attributed to such nature of the LUMO.[25,63]

For **T2**, the INDO/S−SCI calculated absorption spectrum is shown in Figure 13b, and the transition properties of the lowest 18 singlet excited states are summarized in Table 3. Based on the present calculation, the Q_x, B_x, and B_y absorption bands in the T2 spectrum are assigned to the $1B_{3u}$, $2B_{3u}$, and $4B_{2u}$ states (in the D_{2h} notation), respectively, indicating that the transition dipole moment is parallel to the long molecular x axis for the Q_x and B_x bands, whereas it is aligned along the short molecular y axis for the B_y band. Although the splitting of the monomer's

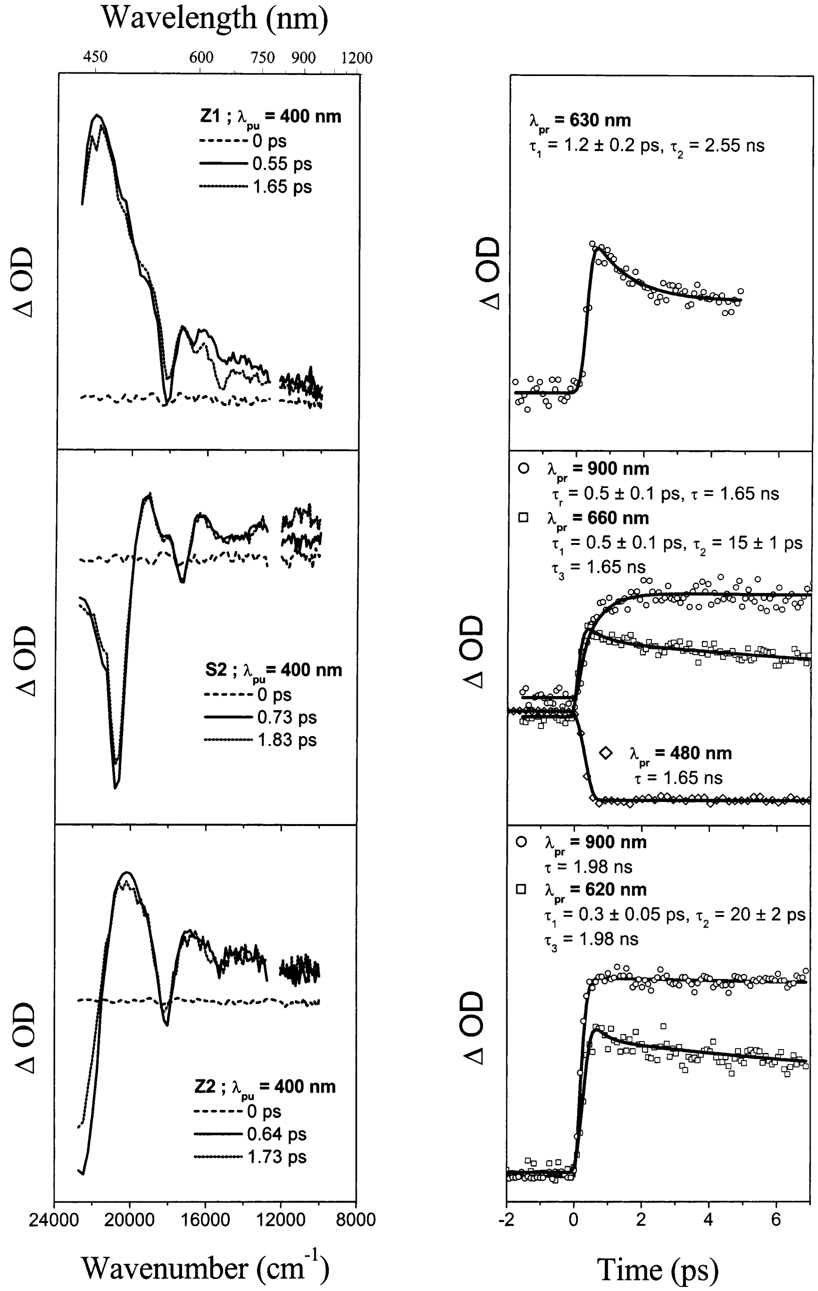

Figure 11. Transient absorption spectra of Z1 (top), S2 (middle), and Z2 (bottom) at three time delays after photoexcitation at 400 nm (left). The transient absorption temporal profiles and fitting results were shown (right). Reproduced with permission from ref 23d.

B band into the B_x and B_y bands is consistent with the exciton-coupling scheme, the CT character of the $2B_{3u}$ and $4B_{2u}$ states is significantly enhanced as compared with the corresponding excited states of meso−meso linked Zn(II) diporphyrin.[23] For the SCI expansion of the $1B_{3u}$ state (Q_x band), the contribution of the HOMO to LUMO transition amounts to 72%, whereas that of the HOMO-1 to LUMO+1 transition is only 15%. Then, the overall transition dipole moment of this state is dominated by that of the former resulting in the markedly intensified Q_x band as compared with the Q(0,0) band of the porphyrin monomer which is very weak due to a mutual cancellation of transition dipole moments of nearly degenerate $^1(a_{1u}, e_g)$ and $^1(a_{2u}, e_g)$ configurations. The intensification as well as the red-shift of the Q_x band of T2 can be attributed to the above-mentioned orbital splitting which is caused by efficient π conjugation through the triple linkage.

In the energy region between the B_x and B_y bands, at least two absorption bands are detected at ca. 458 and 515 nm. We assign these absorption bands to the $3B_{3u}$ (CT_x band) and $2B_{2u}$ (CT_y band) states, respectively. The low-energy intersubunit CT states are described as a one-electron transition from the a_{1u} or a_{2u} MO of one unit to one of the e_g MOs of the other unit. In the previous INDO/S−SCI study on meso−meso linked diporphyrin,[23] we found that such eight CT states are accidentally located in the energy region spanned by the split B bands. Because such a situation should be caused by a close proximity of the constituent porphyrin subunits, it is also expected for T2. Although a complete assignment of all eight CT states is difficult for T2 because of a significant mixing of localized exciton (LE) and CT nature in the excited states, the $2B_{2u}$ can be unambiguously assigned to one of such CT states based on its P_{CT} and W_8 values (Table 3). On the other hand, the $3B_{3u}$ state (CT_x band) can be hardly described by transitions within eight orbitals and the contribution of the HOMO-4 to the LUMO

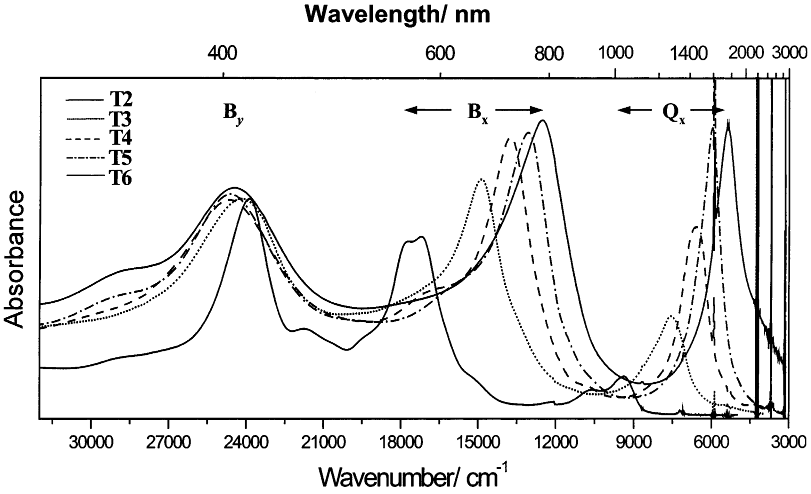

Figure 12. Ultraviolet−visible-infrared absorption spectra of the fused porphyrin arrays from T2 to T6 in $CHCl_3$ at room temperature. The background absorptions at ∼6000, ∼4000, and ∼3500 cm^{-1} arise from the overtones of C−H vibration of the solvent.

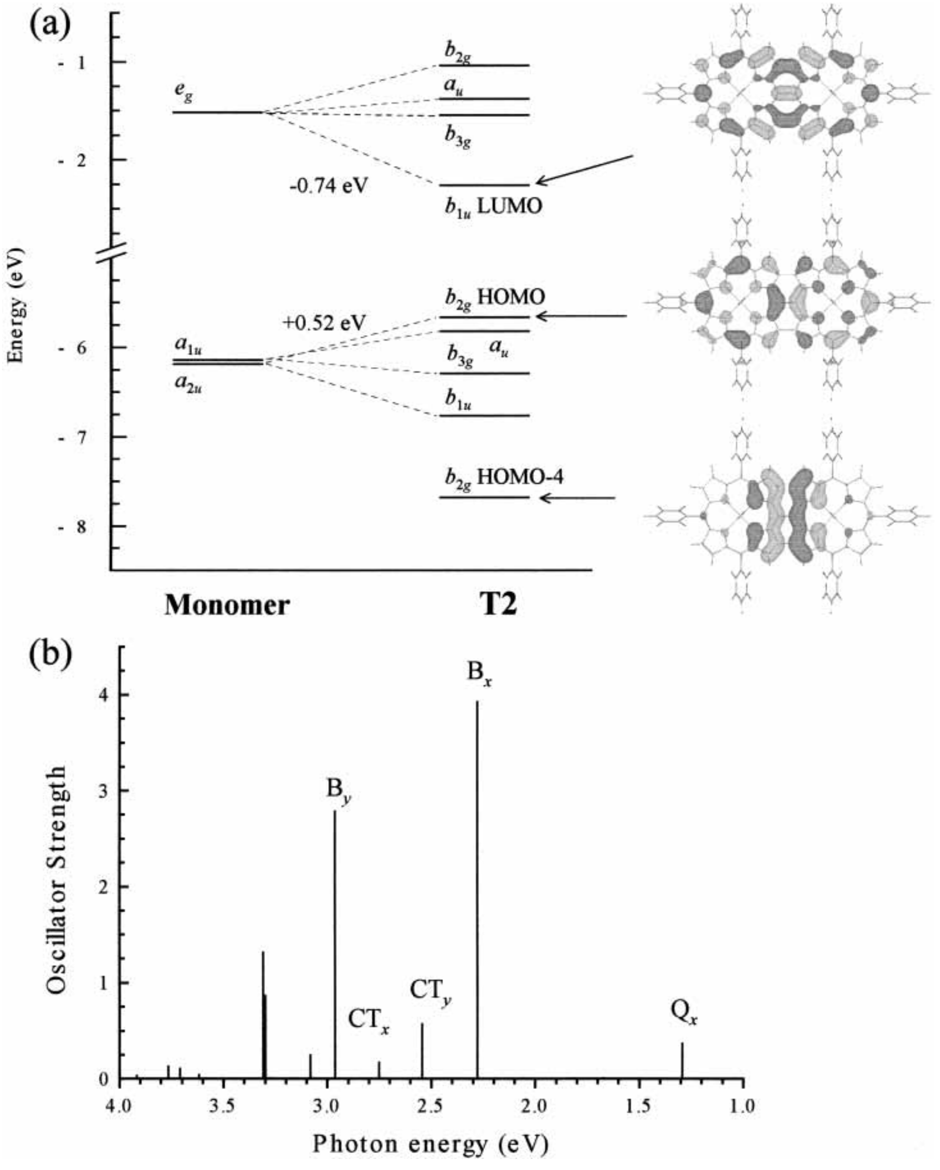

Figure 13. (a) Energy levels of frontier orbitals of T2 compared with those of the monomer as obtained by the INDO/S calculations. Shown in the right panel are the orbital patterns of HOMO-4, HOMO, and LUMO of T2. (b) The INDO/S−SCI simulated electronic absorption spectrum of T2.

transition amounts to 60% in its SCI description; the orbital pattern of the HOMO-4 is also depicted in Figure 13a. The admixing of such a low-lying orbital would be due to a significant configuration mixing which is caused by efficient π

TABLE 3: Transition Properties and Electronic Structures of the Lowest 18 Singlet Excited States of T2, as Obtained from PPP−SCI Calculations.

band	state	ΔE (eV)[a]	f[b]	P_{CT}(%)[c]	W_8(%)[d]	comments[e]
Q_x	$1B_{3u}$	1.41 (1.16)	0.517 (x)	33	96	Q
	$1B_{1g}$	1.52	0	34	97	Q
	$1B_{2u}$	1.77	0.002 (y)	21	97	Q
	$2A_g$	1.98	0	12	96	Q
	$2B_{1g}$	2.24	0	33	81	
B_x	$2B_{3u}$	2.65 (2.13)	3.922 (x)	23	93	Soret
	$3A_g$	2.72	0	68	93	CT
	$2B_{2u}$	2.79	0.694 (y)	68	93	CT
	$3B_{3u}$	2.88	0.382 (x)	46	19	CT
	$3B_{1g}$	3.04	0	59	52	
	$4A_g$	3.15	0	81	90	CT
	$3B_{2u}$	3.21	0.153 (y)	67	92	CT
	$4B_{3u}$	3.22	0.215 (x)	76	75	CT
	$4B_{1g}$	3.38	0	57	52	
	$5B_{3u}$	3.61	1.032 (x)	21	22	
B_y	$4B_{2u}$	3.64 (2.97)	3.415 (y)	9	73	Soret
	$5B_{1g}$	3.68	0	13	69	Soret
	$5A_g$	3.68	0	11	83	Soret

[a] Excitation energy. The experimental values are listed in parentheses. [b] Oscillator strength. The direction of transition dipole moment is indicated in parentheses. [c] Interunit charge-transfer probability defined by $P_{CT} = \sum_{I\neq J}\sum_{r\in I}\sum_{s\in J} P_{e-h}(r,s)$, where I and J represent one porphyrin subunit in a dimer. [d] The weight of the transitions within eight-orbitals in the SCI wave function. [e] The excited states arising from monomer's Q and Soret states are labeled by "Q" and "Soret", respectively. For the explanation of "CT", see Appendix 1.

(a) Exciton Model

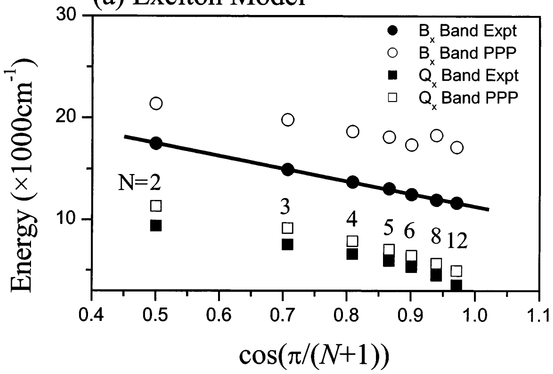

(b) Particle in a Box Model

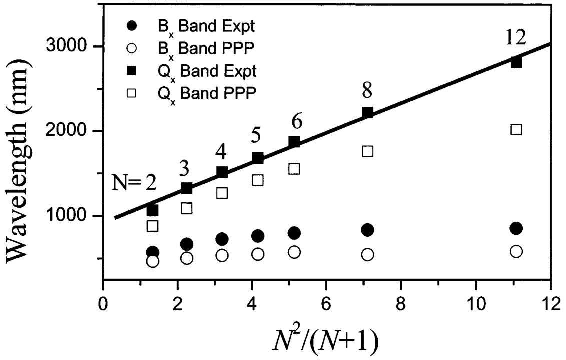

Figure 14. Plots of the energies of the absorption bands B_x and Q_x of T*n* as a function of the number of porphyrin units show a good correlation between the experimental data and PPP−SCI calculated values. The electronic character of the B_x band is explained by the splitting energy of the exciton model (a), whereas that of the Q_x band is well fitted by a particle in a box model (b). Reproduced with permission from ref 25e.

conjugation in T2. For longer arrays, the CT states of both origins described above establish a band of intermediate levels between the B_x and B_y bands with moderate oscillator strengths being responsible for the enhanced absorption in the corresponding energy region (Figure 12).[25]

Electronic Transitions of Fused Porphyrin Arrays. The extensive π conjugation is evident for T*n* in view of more red-shifted absorption spectra and very flat molecular shapes that ensure the coplanarity of the π orbitals of the constituent porphyrin subunits. The observed linear plot of the energy based on eq 1 indicates that the absorption spectral shapes are actually influenced by the number of porphyrin units and the constituent porphyrin pigments are aligned in a regular arrangement in the series (Figure 14a).[25] On the contrary, the plot of the Q_x bands deviates strongly from the exciton coupling scheme. Instead, the plot based on a free electron model (a particle in a box model) gives rise to a well-correlated straight line, indicating that the excited state corresponding to the Q_x band can be characterized by the extensive π conjugation throughout the entire porphyrin arrays (Figure 14b).[25] In addition, our calculation shows that the B_x band comprises several dominant transitions and the B_y band consists of many absorption bands especially for longer arrays. These computational results are consistent with more significant broadening observed for the B_y and B_x bands (especially the former) as compared with the Q_x band. These spectral features indicate efficient π-electron delocalization in the porphyrin arrays, because a simple dipole−dipole interaction between the Soret transitions on the adjacent chromophores should lead to much sharper bandwidth.

The P_{e-h} plots for the excited states of Z8 and T8 are shown in Figure 15, showing how much each state has the CT character. As expected, all three bands of Z8 exhibit largely the LE nature (Figure 15a). Essentially, the LE nature of the B_x state of T8 with less significant contribution of long-range CT is clearly evidenced by the P_{e-h} plot (Figure 15b). Then, it may be considered that significant configuration interaction between LE and CT configurations gives rise to many excited states around the B_x band position (Figure 12). Although the B_y band is dominated by a single excited state up to T4, we find that its CT character is progressively enhanced with an increase in the number of porphyrin subunits based on the P_{e-h} plot for these excited states. For T6, T8, and T12, the B_y band clearly exhibits resonant feature in consistent with the enhancement of CT contribution. The P_{e-h} plot for the B_y states of T8 exhibits intermediate CT character among the main twelve component states. On the basis of the average over the component states, we can say that the CT character of the B_y band is more significant than that of the B_x band.

As seen from the P_{e-h} plot, the Q_x states of T*n* can be characterized by a charge-transfer exciton being qualitatively similar to the case of the lowest dipole-allowed singlet excited state of π-conjugated polymers such as poly(*p*-phenylene vinylene) (PPV).[64] Thus, T*n* does not show any indication of ECL effect, suggesting further lowering of the band gap energy in even longer arrays.

Resonance Raman Spectra of Fused Porphyrin Arrays. The RR spectra of a series of fused porphyrin arrays with photoexcitation at 457.9 nm, which is in resonance with the CT_x ($3B_{3u}$) transitions, are displayed in Figure 16. At first glance, the overall RR spectra of T*n* are quite complicated especially in high-frequency region (1000∼1700 cm^{-1}) as compared with the porphyrin monomer and change quite differently from the RR spectrum of T2 with an increase of the number of porphyrin units in the array.[65] The overall spectral features become simplified in going from T2 to T6, showing mostly polarized RR bands. This reflects that the red-shift of the absorption

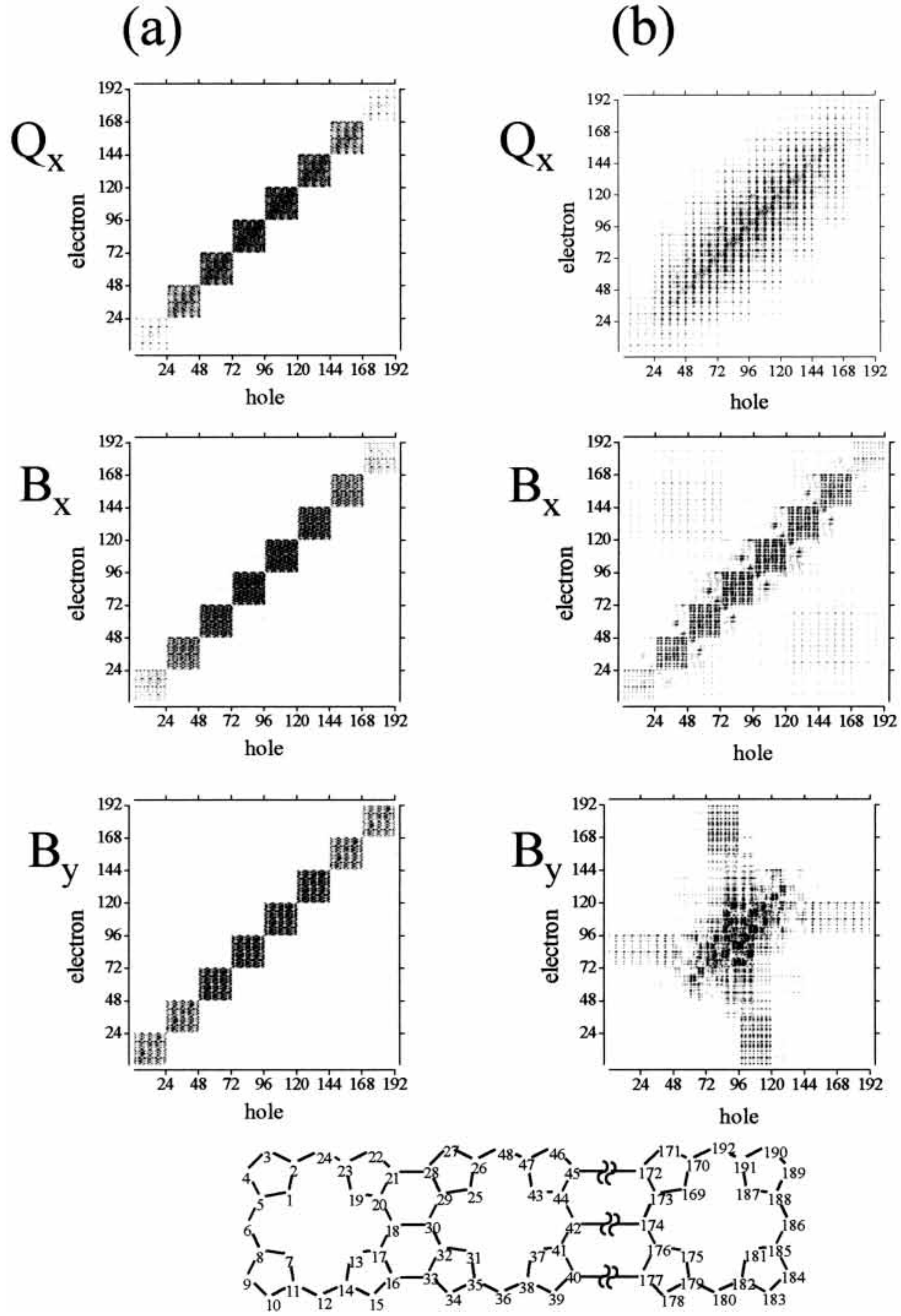

Figure 15. PPP−SCI calculated charge-transfer probability $P_{\mathrm{e-h}}(r,s)$, which is defined by eqs A1-2 and A1-3, for the excited states contributing to the Q_x, B_x, and B_y bands for Z8 (a) and T8 (b). The shading at each grid (r,s) represents the probability of simultaneously finding an electron at *r*th atomic site and a hole at *s*th site. The numbering of atomic sites for T8 is also indicated and the numbering way for Z8 is the same as that for T8. Reproduced with permission from ref 25e.

maximum becomes closer to the resonance excitation line resulting in the RR enhancement of predominantly polarized Raman bands. At the same time, the enormously broadened spectral features explain the observation of a few depolarized RR bands, which are definitely caused by the Herzberg−Teller scattering involving relatively weak CT transitions. The diminishment of the strongest RR band at 1366 cm^{-1} in T2 with an increase of the porphyrin array length is consistent with the very weak RR enhancement of this band in the RR spectrum of T2 by the 416 nm excitation (not shown) that is close to the absorption maximum of the B_y band. The diminishment of the RR bands at 1004, 1270, and 1610 cm^{-1}, which are very strong in the RR spectrum of T2 by the 416 nm excitation, is regarded as representing geometry changes with an increase of the porphyrin array length.

Most of the RR bands of T*n* except the ν_4 (1270 cm^{-1}), ν_{39} (1565 cm^{-1}), and ν_6 (1610 cm^{-1}) modes show frequency shifts as the number of porphyrin units increases. Because the ν_4 mode is localized on meso-carbons parallel to the short molecular axis and the other two modes are localized on the bridge carbons of the dimeric porphyrin ring (Figure 17a), the influence by addition of another porphyrin unit seems to be not so significant.[65] On the other hand, the RR bands showing frequency shifts such as the ν_{17}, ν_{11}, and ν_8 modes include C_{m3}−phenyl, $C_{\beta3}$−$C_{\beta4}$ stretching, and C_β−H bending vibrations (Figure 17b).[65] The frequency shifts of these Raman modes can be

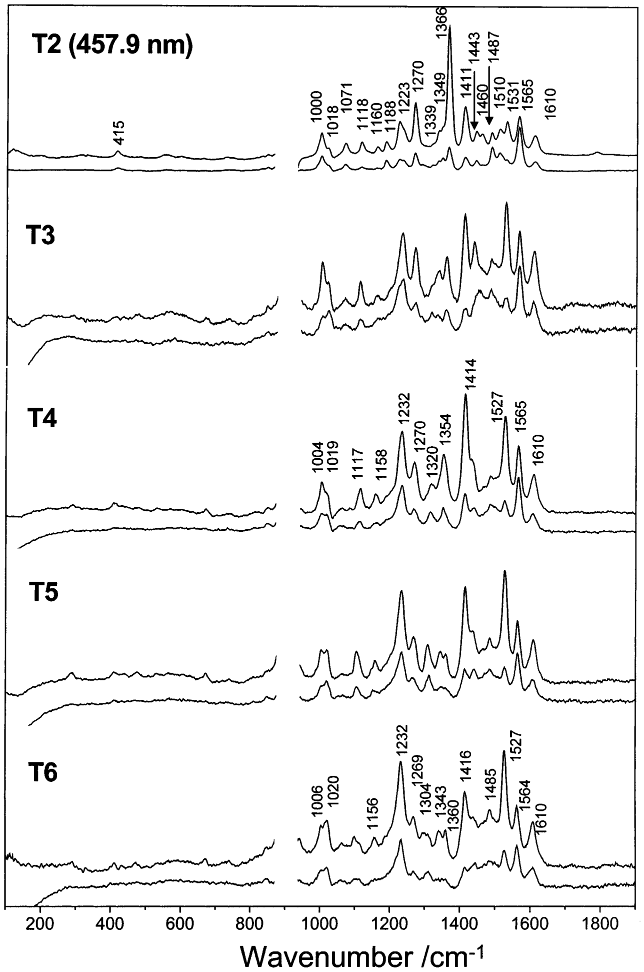

Figure 16. Resonance Raman spectra of T*n* in THF by photoexcitation at 457.9 nm. For each set of spectra, the top and bottom spectra correspond to the parallel and perpendicular polarizations to the incident polarization, respectively.

explained by environmental changes at $C_{\beta3}$, $C_{\beta4}$, and C_{m3} positions (mostly outer carbons of the dimeric porphyrin ring) as the number of porphyrin units increases from T2 to T6. The ν_{17} (1223 cm^{-1}), ν_{11} (1411 cm^{-1}), and ν_8 (1531 cm^{-1}) modes in the RR spectrum of T2 are moderately enhanced. However, these RR bands become gradually stronger in going from T2 to T6. It is noteworthy that these modes involve the vibrations of meso−meso carbons connecting two porphyrin rings as well as adjacent $C_{\alpha1}$ carbons. The $C_{\alpha1}-C_{m1}-C_{\alpha1}$ bending motion yields a normal mode that is delocalized over the fused porphyrin dimer. This feature leads to an enhancement of this mode because of an increase of polarizability.[66] On the contrary, the 1610 cm^{-1} band involving the $C_{\beta1}-C_{\beta1'}$ stretching vibration maintains its intensity as the number of porphyrin units increases. Accordingly, because the $C_{\beta1}-C_{\beta1'}$ stretching vibration is localized on the linking part of T2, this mode does not contribute to the delocalization of the molecular vibrations throughout the fused dimer (Figure 17a). It is interesting to note that the low-frequency RR bands below 800 cm^{-1} are largely diminished in the RR spectra of Tn. In the RR spectrum of the porphyrin monomer, most of the low-frequency RR bands involve out-of-plane modes of porphyrin macrocycle. The lack of out-of-plane vibrational modes in T*n* is likely to arise from the completely flat molecular structures of T*n*. Collectively, our data from the RR spectroscopic measurements as well as the quantum chemical calculations provide a clear picture on the electronic transitions in relation to the molecular structures of T*n*.

Excited-State Dynamics of Fused Porphyrin Arrays. To explore the excited-state dynamics of T*n*, we carried out the femtosecond pump/probe experiments for T2∼T6. Figure 18 shows a series of temporal profiles with a systematic change in the pump wavelengths to be in resonance with the B_x and Q_x states. The bleaching recovery processes at the B_x bands thus monitored are in a good agreement with each other and similar to those by the B_y excitation (not shown),[25e] indicating that the internal conversion processes from the B_y to Q_x states through the B_x state are extremely fast. The femtosecond IR pump/IR probe experiments were also conducted. The temporal profiles of T3 probed at 1400 nm with photoexcitation at the same wavelength show a similar decay to that monitored at 670 nm. However, the measurement of the recovery times of the IR bleaching signals of the porphyrin arrays longer than T4 was severely perturbed by the enhanced transient absorption signal in the IR region. For even longer porphyrin arrays such as T8 and T12, an oxidative decomposition of these arrays at room temperature is likely to prohibit obtaining the reliable transient absorption data.

As the arrays become longer, the number of Soret and CT states increases in proportion to the number of porphyrin subunits in T*n*. Because the CT bands are essentially located in the high-energy side of the B_x band, the density of states is much higher in the energy region between the B_y and B_x bands than that between the B_x and Q_x bands (Table 3). These computational results are consistent with the absorption spectra of T*n* which shows more significantly enhanced absorption in the interval wavelength region between the B_y and B_x bands than that between the B_x and Q_x bands. Therefore, on the basis of the orientation of the transition dipoles of the electronic transitions and the PPP−SCI calculations, the rate determining step in the overall internal conversion processes upon photoexcitation of the B_y states in T*n* is likely to be the $B_x \rightarrow Q_x$ internal conversion process as observed by the transient absorption anisotropy measurement in T2.[25] However, it becomes more difficult to determine the bottleneck step in the internal conversion process as the array becomes longer, because the energy gap between the B_x and Q_x states becomes reduced and the intermediate states between the two states increase as observed in the absorption spectra.

The energy relaxation dynamics of the lowest excited states of T*n* are much accelerated as the number of attached porphyrin units increases, which is consistent with the energy gap law (Figure 18b).[67] The lowest excited electronic state of T2 decays to the ground state with the time constant of 4.5 ps, which is much faster than that of the orthogonal dimer (1.98 ns). Upon elongation of the porphyrin arrays, the decay times of the lowest excited electronic states decrease significantly, 2.3 ps for T3, 0.4 ps for T4, 0.3 ps for T5, and 0.3 ps for T6. In sharp contrast, the lifetimes of the lowest excited electronic states of Z1∼Z6 are in a range of 2.55∼1.66 ns. The decay rates of the Q_x states of T*n* are enhanced as the Q_x state energies are lowered, indicating that there is a strong correlation between the ordering of the Q_x state energies and that of their lifetimes.

The absorption spectra of T*n* show that the absorption tail of the Q_x band becomes gradually wider, indicating the increased density of states near the lowest excited states (Figure 12). In addition, the absorption 0−0 band downshifts from 9400 cm^{-1} for T2 to 5300 cm^{-1} for T6. Thus, the combination of the reduced energy gap and the increased density of states near the

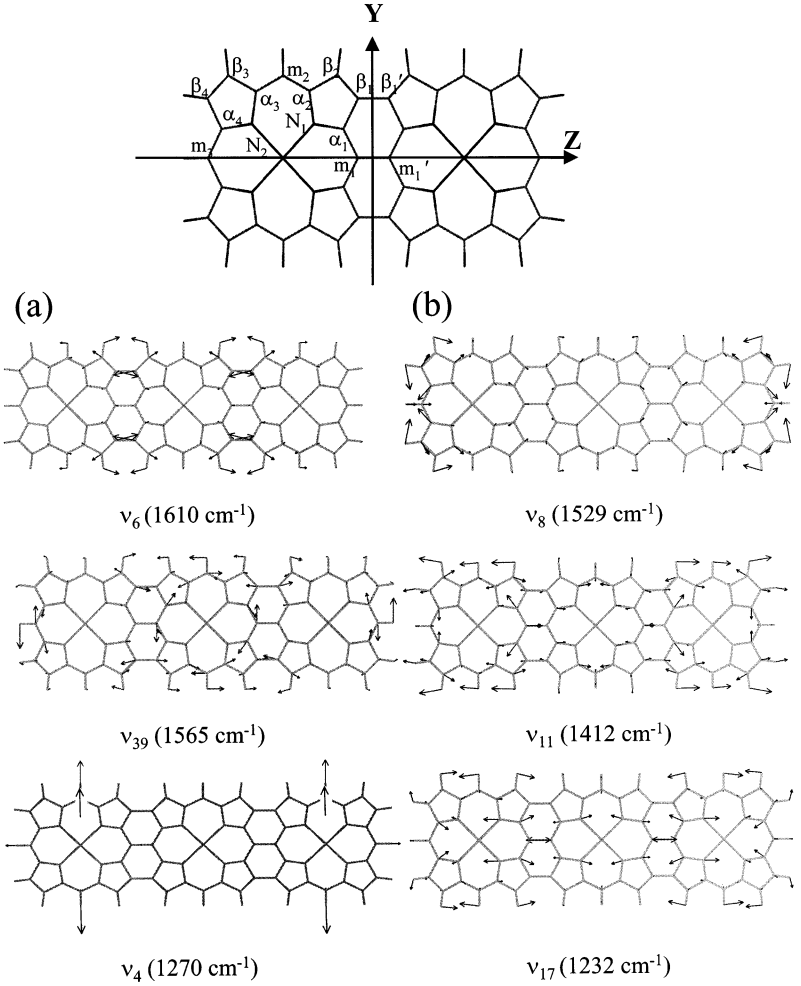

Figure 17. Axis notation and the atomic labeling scheme (top). Representative vibrational eigen vectors of T3 without phenyl substituents (bottom).

lowest excited states is likely to facilitate the electronic deactivation processes from the lowest excited state to the ground state as T*n* becomes longer. At the same time, because the energy difference between the lowest excited and ground states becomes significantly reduced in T*n*, the vibronic coupling process becomes enhanced. This process provides more effective nonradiative deactivation channels for longer arrays because they have rich vibrational motions that can couple to the electronic states as the electronic energy levels become lowered.

Optical Nonlinear Materials Based on Porphyrin Arrays. Not only as nonlinear optical materials but also as molecular electric wires and IR sensors, T*n* could open up new opportunities in molecular electronics. Thus, nonlinear optical properties of T*n* as well as Z*n* were comparatively investigated using a Z-scan method, in which a single Gaussian beam was employed for inducing and probing light-induced complex refractive index change.

Figure 19 shows the typical data for open-aperture (upper), and closed aperture (lower) Z-scan measurements for (a) T*n* and (b) Z*n*. The results for the real part of nonlinear refractive index γ were plotted as a function of the number of porphyrin units in T*n* and Z*n*. The γ value of the porphyrin monomer was reported to be on the order of $\sim 10^{-31}$ esu at 532 nm.[68] Thus, it is expected to be much smaller at 1064 nm, further away from the absorption band, and we observed the γ value of the order of $\sim 10^{-34}$ esu, of which even the sign is undeterminable due to the detection limit.

T*n* exhibits the optical nonlinearity values larger by about an order of magnitude than Z*n* with the same number of monomer units (Figure 20). As the number of monomer units increases in Z*n* and T*n*, the optical nonlinearity at first increases but quickly becomes saturated at 3$\sim$4 monomer units. One can consider the optical nonlinearity per monomer unit in Z*n* and T*n* as a measure of π-electron delocalization along the neighboring units. The results show that the optical nonlinearity per monomer unit remains nearly constant throughout $n = 2\sim 8$, indicating that π electrons cannot move too much beyond the neighboring units at 1064 nm excitation. This is similar to the case of π-conjugated polymer showing the saturation effect in nonlinear susceptibility. For instance, the γ values of thiophene oligomers were reported to increase with an increase in thiophene units, but the γ value per unit is saturated at approximately 4 monomer units.[69]

Unlike the 1064 nm case, both types of the porphyrin arrays had large linear absorption coefficients at 532 nm. Unfortunately, it is suspected that T*n* became disintegrated or aggregated by laser light and permanently stuck to the cuvette wall during a single Z-scan measurement even under the lowest laser intensity where the nonlinearity of THF solvent can be measured reliably. Thus the Z-scan experiment was done only for Z*n* at 532 nm (Figure 20). For the same number of porphyrin units in the array, the nonlinearity at 532 nm is roughly 2 orders of magnitude larger than that at 1064 nm, and the numbers are in a good agreement with the previous results.[69] The γ value at this wavelength also increases with the number of porphyrin units and becomes slowly saturated around at $n = 6$. The per-monomer γ shows a similar behavior as in the 1064 nm case,

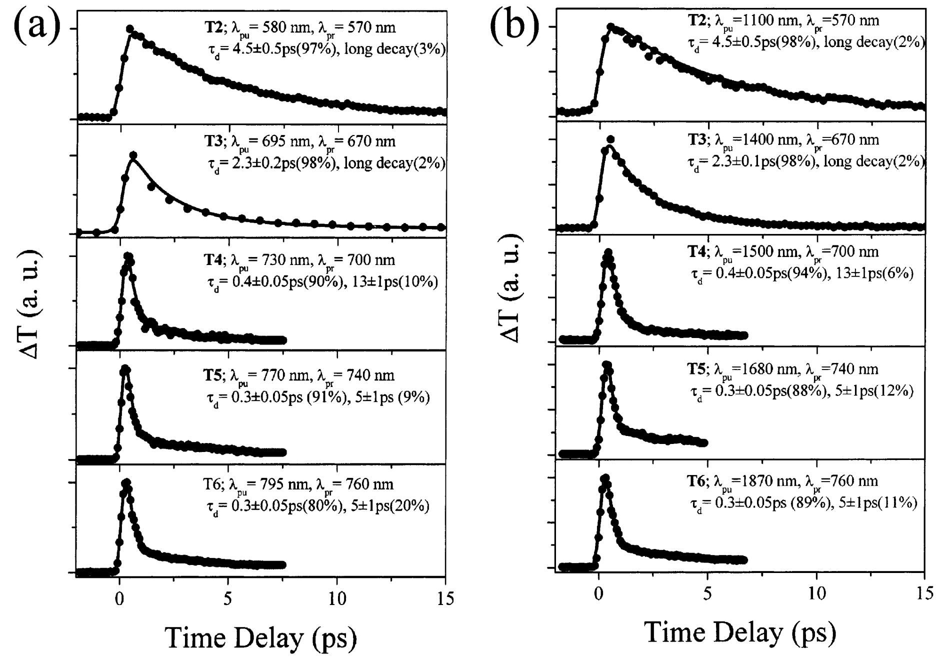

Figure 18. (a) Ground-state bleaching recovery dynamics of T2 (top) to T6 (bottom) probed at the B_x bands after photoexcitation at the B_x bands. The ground state bleaching recovery time is gradually accelerated in going from T2 to T6, showing a saturation effect in the arrays longer than T4. The time constants and pump/probe wavelengths are depicted in the inset. (b) Ground-state bleaching recovery dynamics of T2 (top) to T6 (bottom) probed at the B_x bands after photoexcitation at the Q_x bands. The ground state bleaching recovery time is gradually accelerated in going from T2 to T6, showing a saturation effect in the arrays longer than T4. The time constants and pump/probe wavelengths are depicted in the inset. Reproduced with permission from ref 25e.

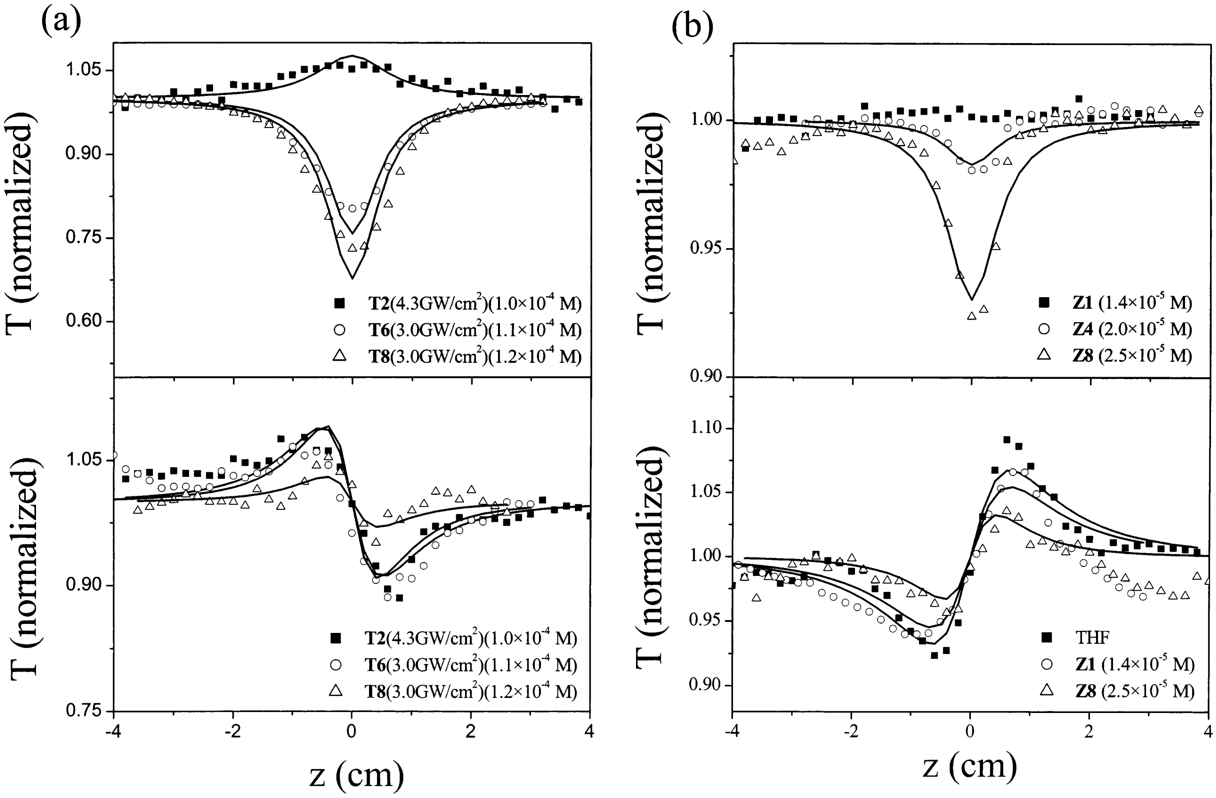

Figure 19. (a) Open-aperture Z-scan data (upper) and closed-aperture Z-scan data (lower) of T*n* in THF at 1064 nm. (b) Open-aperture Z-scan data (upper) and closed-aperture Z-scan data (lower) of Z*n* in THF at 1064 nm.

indicating the extension of π-electron delocalization should be within a few porphyrin units nearby irrespective of the array length.

Electrical Conduction through Linear Porphyrin Arrays. The electronic structure of porphyrin arrays is closely related to the electronic overlap between π-conjugated systems.[70] In this regard, we have comparatively measured the electrical transport properties of Z48 and T8 to investigate the influence of electronic interactions between the adjacent porphyrin molecules. To measure the electrical transport properties of porphyrin arrays directly, two kinds of Au/Ti nanoelectrodes were prepared. For the orthogonal porphyrin array with a length

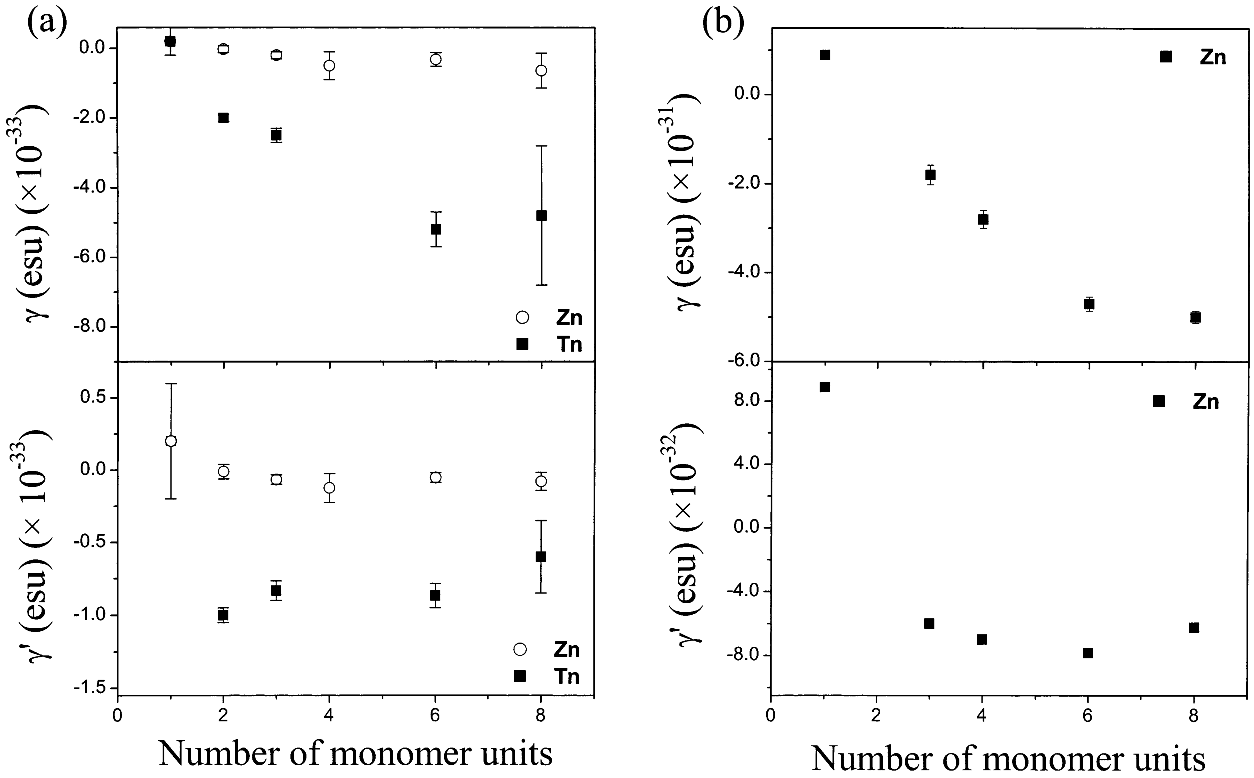

Figure 20. (a) Molecular nonlinear susceptibility γ (upper) and γ per monomer unit (γ') (lower) vs the number of monomer units for Z*n* and T*n* at 1064 nm. (b) Molecular nonlinear susceptibility γ (upper) and γ per monomer unit (γ') (lower) for Z*n* at 532 nm.

of about 40 nm, the nanoelectrodes with a spacing of about 20−30 nm were fabricated by electron-beam lithography and double-angle evaporation technique onto degenerately doped silicon substrate with a top SiO_2 layer of 0.5 μm. On the other hand, for the fused porphyrin array with about 7 nm in its length, the Au/Ti nanoelectrodes with a spacing of less than 7 nm were prepared by utilizing the electromigration induced break-junction technique.[71] Electrical contact between porphyrin arrays and metal electrodes was made using the electrostatic trapping method.[70] A drop of porphyrin solution (3 nmol) was positioned on the top of the electrode gap. Then, a voltage of up to 5 V was applied to the electrodes. After trapping the porphyrin array between the electrodes, the sample was dried under nitrogen purging and characterized using a semiconductor characterization system (Keithley 4200). All electrical transport measurements were performed in a vacuum to eliminate the effect of water on the conductance.

Figure 21a displays the *I*−*V* curve measured at room temperature for Z48 trapped between two nanoelectrodes. It exhibits the diode-like behavior and the hysteresis depending on the voltage sweep direction. We have also measured the *I*−*V* curve under illumination with a red LED (not shown). The conductance was enhanced under illumination. Similar photocurrent effects have been also observed by Liu et al.[72] in porphyrin films. However, the hysteresis was found in both *I*−*V* curves. Although the origin of the observed hysteresis is not clear, we speculate that it is probably attributed to the rotation about the meso−meso C−C bond in the orthogonal porphyrin array, because the theoretical AM1 calculation has shown that the dihedral angle between porphyrin rings varies approximately from 70° to 110° at room temperature and the electrical conductivity is expected to depend on the distribution in the dihedral angle between the adjacent porphyrin rings. We have also measured the *I*−*V* curve as the temperature decreases. The hysteresis was observed to disappear at 200 K, supporting our speculation that the hysteresis is due to the conformational heterogeneity arising from the dihedral angle distribution. In addition, the conductance decreased very rapidly with lowering temperature and no current was measured in the voltage range from −5 to +5 V even at 180 K.

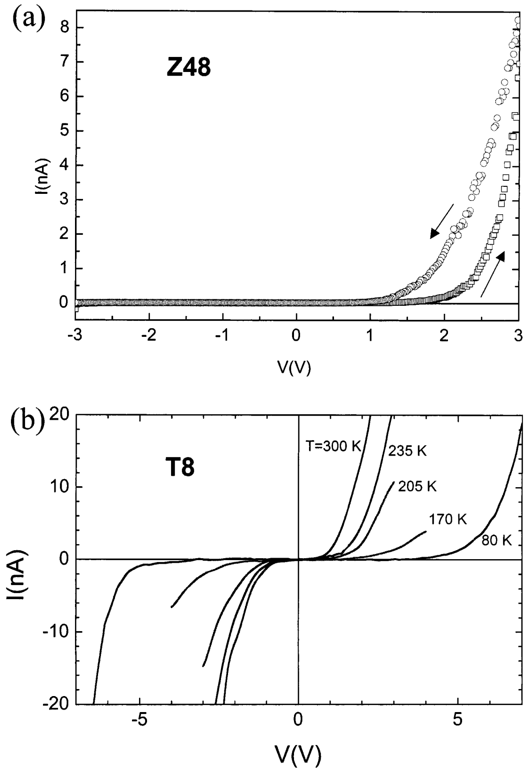

Figure 21. (a) *I*−*V* curves of Z48 trapped between two metal electrodes measured at room temperature. (b) The *I*−*V* curves of T8 trapped between two metal electrodes measured at various temperatures.

Figure 21b shows the $I-V$ curve measured at several temperatures for T8. In contrast to Z48, it is nearly symmetric without any hysteresis, implying that the rotation about the meso−meso C−C bond is hindered in the fused porphyrin array. Moreover, the higher conductivity[73] and the smaller voltage gap were found compared with Z48. These results indicate that the stronger π conjugation of T8 results in the better electrical conduction because of the smaller HOMO−LUMO band gap. As the temperature decreases, the conductance decreases and the voltage gap widens. However, it should be noted that the temperature dependence is much slower than that of Z48.

VI. Conclusions

A variety of porphyrin arrays have been prepared and investigated for the applications in molecular photonics and electronics. The elucidation of the interporphyrinic interactions in diporphyrins by controlling the dihedral angle between the two porphyrin planes has provided a firm basis for a deep understanding of the excitonic interactions in long porphyrin arrays. A failure of the exciton coupling scheme in explaining the absorption spectra of S*n* suggests the existence of the charge-transfer transitions residing at the similar energy regions to the exciton Soret bands of S*n*. In Z*n* and T*n* the contributions of CT transitions to the absorption spectra are responsible for the broad excitonic bands and the enhanced absorption in the intermediate regions between the excitonic bands. Z*n* is promising in the application as a photonic wire because of the exceptionally strong excitonic interactions between the neighboring porphyrin moieties arising from a close proximity with a reasonably long length. On the other hand, T*n* has proven to be a good optical nonlinear material induced by extensive π-electron delocalization throughout the entire T*n* arrays. However, the preparation of even longer T*n* arrays is still highly desirable for the real application as optoelectronic devices in the future.

Appendix 1

Within the SCI scheme, the atomic-orbital (AO) representation, which is equivalent to the site representation under the PPP approximation,[56] of the transition density matrix corresponding to an excited state is given by

$$\rho_{rs} = \langle e|a_r{}^{+}a_s|g\rangle = \sqrt{2}\sum_i \sum_a Y_i^a(e)C_{\mathrm{ri}}C_{sa} \qquad \text{(A1-1)}$$

where $a_r{}^{+}$ creates an electron at rth AO, $\boldsymbol{e}$ represents the SCI excited state, and g is the Hartree−Fock ground state. $Y_i^a(e)$ is the SCI expansion coefficient associated with i (occupied MO) to a (unoccupied MO) transition and C_{ri} is the LCAO (linear combination of AO) coefficient in ith MO. To characterize each excited state in terms of charge-transfer (CT) nature, we calculate the charge-transfer probability $P_{\mathrm{e-h}}\,(r,s)$ defined by

$$P_{\mathrm{e-h}}\,(r,s) = \rho_{\boldsymbol{rs}}{}^2/2 \qquad \text{(A1-2)}$$

which represents the probability of simultaneously finding an electron at r and a hole at s.[64] Note that the orthonormalization of AOs assumed in the present scheme ensures $\sum_{r,s} P_{\mathrm{e-h}}(r,s) = 0$. We define the interunit CT probability by

$$P_{\mathrm{CT}} \equiv \sum_{I\neq J}\sum_{r\in I}\sum_{s\in J} P_{\mathrm{e-h}}(r,s) \qquad \text{(A1-3)}$$

where I and J represent each porphyrin subunit in a dimer.

Appendix 2

The simple quantum mechanics treats the energy transfer processes with the time-dependent perturbation theory. The unperturbed lowest exciton state specified by $|d\rangle$ can be written as a linear combination of each excited state $|n\rangle$ of the nth porphyrin in the donor molecules as follows:

$$|d\rangle = \sqrt{\frac{2}{N+1}}\sum_{n=1}^{N}\sin\left(\frac{\pi}{N+1}n\right)|n\rangle \qquad \text{(A2-1)}$$

where N is the number of porphyrin units in the donor. Its energy eigenvalue (E_d) is given by

$$E_d = E_A + 2\Delta\cos\left(\frac{\pi}{N+1}\right) \qquad \text{(A2-2)}$$

where E_A is the excited energy of the isolated porphyrin monomer, and Δ is the interaction energy of the neighboring porphyrins.

The final state of energy transfer is written as $|a\rangle$, which represents the excited state of the acceptor molecule. The Hamiltonian for the excited states on the array is given by

$$H' = \sum_{n=1}^{N} J_n(|a\rangle\langle n| + |n\rangle\langle a|) \qquad \text{(A2-3)}$$

where J_n is the electrostatic interaction between nth donor molecule and acceptor in the EET state. Because J_n is proportionate with the third power of the distance in the dipole−dipole calculation, J_n is given by

$$J_n = J_1\left(\frac{R_1}{R_n}\right)^3 \qquad \text{(A2-4)}$$

where R_n represents the distance between nth donor molecule and acceptor. The EET interaction between the initial state and the final state is given by

$$\begin{aligned} J \equiv \langle a|H'|d\rangle = \sqrt{\frac{2}{N+1}}\sum_{n=1}^{N} J_n \sin\left(\frac{\pi}{N+1}n\right) = \\ \sqrt{\frac{2}{N+1}}\,J_1\sum_{n=1}^{N}\left(\frac{R_1}{R_n}\right)^3\sin\left(\frac{\pi}{N+1}n\right) \qquad \text{(A2-5)} \end{aligned}$$

According to the time-dependent perturbation theory of quantum mechanics, the well-known expression for the transition rate constant[74] is

$$k_N = \frac{2\pi}{\hbar}J^2\int I_{\mathrm{a}}(\upsilon)L_{\mathrm{d}}(\upsilon)\,\mathrm{d}\upsilon \qquad \text{(A2-6)}$$

where $I_{\mathrm{a}}(\upsilon)$ and $L_{\mathrm{d}}(\upsilon)$ is the spectral distribution of absorption of acceptor and fluorescence of donor, respectively, and they are normalized. Equation A2-6 is the other representation of Förster formula, in which energy transfer operates via Coulombic interaction between transition dipole moments and therefore requires no direct contact between energy donor and acceptor, the rate of singlet energy transfer can be expressed in terms of the center-to-center distance (R) between the two transition dipole moments. Here, the number dependency of fluorescence was boldly ignored from the eqs A2-5 and A2-6. Finally, the energy transfer rate is depicted as follows:

$$k_N \approx \frac{2}{N+1}\left[\sum_{n=1}^{N}\left(\frac{R_1}{R_n}\right)^3\sin\left(\frac{\pi}{N+1}n\right)\right]^2 k_1 \qquad \text{(A2-7)}$$

Equation A2-6 appears to be similar to Förster's formula in terms of its dependence on the spectral overlap integral between the acceptor state and the donor state but is critically different from Förster's formula in the expression of J, because it is given in eq A2-5 by a sum of terms inversely proportional to the third power of the distance R_n between the nth molecule in the donor aggregate and the acceptor molecule. If all R_n's are much larger than R_1, they could be approximated by an average distance R between the donor aggregate and the acceptor molecule, and eq A2-6 would reduce to Förster's formula, becoming inversely proportional to R^6. In reality, however, the R_n varies from R_1 to a value considerably larger than R_1, and eq A2-6 gives a magnitude much different from that given by Förster's formula. Such a difference arises from the size effect of the molecular aggregate for the donor state in the present systems. Because J_n in eq A-5 for J arises from the long-distance transition-dipole interaction between two molecules, no direct contact between them is required in eq A2-6, being similar to Förster's formula.

Acknowledgment. This work has been financially supported by the National Creative Research Initiatives Program of the Ministry of Science & Technology of Korea. The work at Kyoto was supported by CREST (Core Research for Evolutional Science and Technology) of Japan Science and Technology Corporation (JST). The authors express their sincere gratitude to the talented graduate students, postdoctoral fellows, and collaborators listed as coauthors in the references involved in elaborate synthesis of various porphyrin molecules and very sophisticated measurements of their photophysical properties. Finally, special thanks are extended to Drs. Dae Hong Jeong and Jae Kyu Song for their help in the preparation of this manuscript.

References and Notes

(1) Ratner, M. A.; Jortner, J. *Molecular Electronics*; Jortner, J., Ratner, M. A., Eds.; IUPAC, Blackwell Science: Cambridge, MA, 1997; Chapter 1.

(2) Holten, D.; Bocian, D. F.; Lindsey, J. S. *Acc. Chem. Res.* **2002**, *35*, 57 and references are therein.

(3) (a) Gosztola, D.; Yamada, H.; Wasielewski, M. R. *J. Am. Chem. Soc.* **1995**, *117*, 2041. (b) Debreczeny, M. P.; Svec, W. A.; Marsh, E. M.; Wasielewski, M. R. *J. Am. Chem. Soc.* **1996**, *118*, 8174. (c) Debreczeny, M. P.; Svec, W. A.; Wasielewski, M. R. *Science* **1996**, *274*, 584. (d) van der Boom, T.; Hayes, R. T.; Zhao, Y.; Bushard, P. J.; Weiss, E. A.; Wasielewski, M. R. *J. Am. Chem. Soc.* **2002**, *124*, 9582. (e) Susumu, K.; Therien, M. J. *J. Am. Chem. Soc.* **2002**, *124*, 8550. (f) Takahashi, R.; Kobuke, Y. *J. Am. Chem. Soc.* **2003**, *125*, 2372.

(4) Turek, P.; Petit, P.; Andre, J.-J.; Simon, J.; Even, R.; Boudjema, B.; Guillaud, G.; Maitrot, M. *J. Am. Chem. Soc*. **1987**, *109*, 5119.

(5) Hoffman, B. M.; Ibers, J. A. *Acc. Chem. Res.* **1983**, *16*, 15.

(6) (a) Collman, J. P.; Anson, F. C.; Barnes, C. E.; Bencosme, C. S.; Geiger, T.; Evitt, E. R.; Kreh, R. P.; Meier, K.; Pettman, R. B. *J. Am. Chem. Soc*. **1983**, *105*, 2694. (b) Collman, J. P.; Bencosme, C. S.; Barnes, C. E.; Miller, B. D. *J. Am. Chem. Soc*. **1983**, *105*, 2704. (c) Ni, C. L.; Abdalmuhdi, I.; Chang, C. K.; Auston, F. C. *J. Phys. Chem*. **1987**, *91*, 1158.

(7) (a) Gregg, B. A.; Fox, M. A.; Bard, A. J. *J. Phys. Chem*. **1990**, *94*, 1586. (b) Liu, C.-Y.; Pan, H.-L.; Fox, M. A.; Bard, A. J. *Science* **1993**, *261*, 897.

(8) Anderson, H. L.; Martin, S. J.; Bradley, D. D. C. *Angew. Chem., Int. Ed. Engl.* **1994**, *33*, 655.

(9) (a) Wasielewski, M. R. In *Chlorophylls*; Scheer, H., Ed.; CRC Press: Boca Raton, FL, 1991; p 269. (b) LaLonde, D. E.; Petke, J. D.; Maggiora, G. M. *J. Phys. Chem*. **1988**, *92*, 4746. (c) Thompson, M. A.; Zerner, M. C.; Fajer, J. *J. Phys. Chem*. **1990**, *94*, 3820.

(10) (a) Osuka, A.; Maruyama, K. *J. Am. Chem. Soc*. **1988**, *110*, 4454. (b) Eriksson, S.; Källebring, B.; Larsson, S.; Mårtensson, J.; Wennerström, O. *Chem. Phys*. **1990**, *146*, 165. (c) Kobayashi, N.; Numao, M.; Kondo, R.; Nakajima, S.; Osa, T. *Inorg. Chem*. **1991**, *30*, 2241. (d) Martin, P. C.; Arnold, J.; Bocian, D. F. *J. Phys. Chem*. **1993**, *97*, 1332. (e) Bilsel, O.; Milam, S. N.; Girolami, G. S.; Suskick, K. S.; Holten, D. *J. Phys. Chem*. **1993**, *97*, 7216. (f) Kadish, K. M.; Moninot, G.; Hu, Y.; Dubois, D.; Ibnlfassi, A.; Barbe, J.-M.; Guilard, R. *J. Am. Chem. Soc*. **1993**, *115*, 8153.

(11) (a) Ponomarev, G. V.; Borovkov, V.; Sugiura, K.-I.; Sakata, Y.; Shul'ga, A. *Tetrahedron Lett*. **1993**, *34*, 2153. (b) Senge, M.; Gerzevske, K.; Vicente, M.; Forsyth, T.; Smith, K. *Angew. Chem., Int. Ed. Engl*. **1993**, *32*, 750. (c) Ponomarev, G.; Borovkov, V.; Shul'ga, A.; Sakata, Y. *J. Chem. Soc., Chem. Commun*. **1994**, 1927. (d) Senge, M.; Vicente, M.; Gerzevske, K.; Forsyth, T.; Smith, K. *Inorg. Chem*. **1994**, *33*, 5625. (e) Higuchi, H.; Takeuchi, M.; Ojima, *J. Chem. Lett*. **1996**, 593.

(12) (a) Lin, V. S.-Y.; DiMagno, S. G.; Therien, M. J. *Science* **1994**, *264*, 1105. (b) Lin, V. S.-Y.; Therien, M. J. *Chem.-Eur. J*. **1995**, *1*, 645. (c) Rubtsov, I. V.; Susumi, K.; Rubtsov, G. I.; Therien, M. J. *J. Am. Chem. Soc.* **2003**, *125*, 2687.

(13) Arnold, D.; Nitschinsk, L. *Tetrahedron* **1992**, *48*, 8781.

(14) Anderson, H. L. *Inorg. Chem*. **1994**, *33*, 972.

(15) Arnold, D.; Nitschinsk, L. *Tetrahedron Lett*. **1993**, *34*, 693.

(16) Vicente, M. G. H.; Smith, K. *J. Org. Chem*. **1991**, *56*, 4407.

(17) Osuka, A.; Liu, B.-L.; Maruyama, K. *Chem. Lett*. **1993**, 949.

(18) Burrell, A.; Officer, D.; Reid, D. *Angew. Chem., Int. Ed. Engl*. **1995**, *34*, 900.

(19) (a) Osuka, A.; Maruyama, K.; Yamazaki, I.; Tamai, N. *Chem. Phys. Lett*. **1990**, *165*, 392. (b) Osuka, A.; Maruyama, K.; Mataga, N.; Asahi, T.; Yamazaki, I.; Tamai, N. *J. Am. Chem. Soc*. **1990**, *112*, 4958.

(20) Yang, S. I.; Lammi, R. K.; Seth, J.; Riggs, J. A.; Arai, T.; Kim, D.; Bocian, D. F.; Holten, D.; Lindsey, J. S. *J. Phys. Chem. B* **1998**, *102*, 9426.

(21) (a) Osuka, A.; Shimidzu, H. *Angew. Chem., Int. Ed. Engl*. **1997**, *36*, 135. (b) Yoshida, N.; Shimidzu, H.; Osuka, A. *Chem. Lett*. **1998**, 55. (c) Nakano, A.; Osuka, A.; Yamazaki, I.; Yamazaki, T.; Nishimura, Y. *Angew. Chem., Int. Ed. Engl*. **1998**, *37*, 3023. (d) Aratani, N.; Osuka, A.; Kim, D.; Kim, Y. H.; Jeong, D. H. *Angew. Chem*. **2000**, *39*, 1458.

(22) (a) Cho, H. S.; Song, N. W.; Kim, Y. H.; Jeoung, S. C.; Hahn, S.; Kim, D.; Kim, S. K.; Yoshida, N.; Osuka, A. *J. Phys. Chem. A* **2000**, *104*, 3287. (b) Kim, Y. H.; Jeong, D. H.; Kim, D.; Jeoung, S. C.; Cho, H. S.; Kim, S. K.; Aratani, N.; Osuka, A. *J. Am. Chem. Soc*. **2001**, *123*, 76. (c) Kim, Y. H.; Cho, H. S.; Kim, D.; Kim, S. K.; Yoshida, N.; Osuka, A. *Synth. Metal* **2001**, *117*, 183. (d) Aratani, N.; Osuka, A.; Cho, H. S.; Kim, D. *J. Photochem. Photobiol. C: Photochem. Rev*. **2002**, *3*, 25. (e) Min, C.-K.; Joo, T.; Yoon, M.-C.; Kim, C. M.; Hwang, Y. N.; Kim, D.; Aratani, N.; Yoshida, N.; Osuka, A. *J. Chem. Phys*. **2001**, *114*, 6750. (f) Cho, H. S.; Jeong, D. H.; Yoon, M.-C.; Kim, Y.-R.; Kim, D.; Jeoung, S. C.; Kim, S. K.; Aratani, N.; Shinmori, H.; Osuka, A. *J. Phys. Chem. A* **2001**, *105*, 4200.

(23) (a) Yoshida, N.; Osuka, A. *Org. Lett*. **2000**, *2*, 2963. (b) Yoshida, N.; Jeong, D. H.; Cho, H. S.; Kim, D.; Matsuzaki, Y.; Tanaka, K.; Osuka, A. *Chem. Eur. J*. **2003**, *9*, 58. (c) Jeong, D. H.; Jang, S. M.; Hwang, I.-W.; Kim, D.; Yoshida, N.; Osuka, A. *J. Phys. Chem. A* **2002,** *106*, 11054. (d) Cho, H. S.; Song, J. K.; Ha, J.-H.; Cho, S.; Kim, D.; Yoshida, N.; Osuka, A. *J. Phys. Chem. A* **2003**, *107*, 1897.

(24) (a) Martin, R. E.; Diederich, F. *Angew. Chem., Int. Ed. Engl*. **1999**, *38*, 1350. (b) Clar, E. *Ber. Dtsch. Chem. Ges*. **1936**, *69*, 607.

(25) (a) Tsuda, A.; Nakano, A.; Furuta, H.; Yamochi, H.; Osuka, A. *Angew. Chem., Int. Ed*. **2000**, *39*, 558. (b) Tsuda, A.; Furuta, H.; Osuka, A. *Angew. Chem., Int. Ed*. **2000**, *39*, 2549. (c) Tsuda, A.; Furuta, H.; Osuka, A. *J. Am. Chem. Soc*. **2001**, *123*, 10304. (d) Tsuda, A.; Osuka, A. *Science* **2001**, *293*, 79. (e) Cho, H. S.; Jeong, D. H.; Cho, S.; Kim, D.; Matsuzaki, Y.; Tanaka, K.; Tsuda, A.; Osuka, A. *J. Am. Chem. Soc*. **2002**, *124*, 14642.

(26) (a) Li, X.-Y.; Czernuszewicz, R. S.; Kincaid, J. R.; Su, Y. O.; Spiro, T. G. *J. Phys. Chem*. **1990**, *94*, 31. (b) Rush, T. S., III.; Kozlowski, P. M.; Piffat, C. A.; Kumble, R.; Zgierski, M. Z.; Spiro, T. G. *J. Phys. Chem. B* **2000**, *104*, 5020.

(27) Li, X.-Y.; Czernuszewicz, R. S.; Kincaid, J. R.; Spiro, T. G. *J. Phys. Chem*. **1990**, *94*, 47.

(28) Frisch, M. J.; Trucks, G. W.; Schlegel, H. B.; Scuseria, G. E.; Robb, M. A.; Cheeseman, J. R.; Zakrzewski, V. G.; Montgomery, J. A., Jr.; Stratmann, R. E.; Burant, J. C.; Dapprich, S.; Millam, J. M.; Daniels, A. D.; Kudin, K. N.; Strain, M. C.; Farkas, O.; Tomasi, J.; Barone, V.; Cossi, M.; Cammi, R.; Mennucci, B.; Pomelli, C.; Adamo, C.; Clifford, S.; Ochterski, J.; Petersson, G. A.; Ayala, P. Y.; Cui, Q.; Morokuma, K.; Malick, D. K.; Rabuck, A. D.; Raghavachari, K.; Foresman, J. B.; Cioslowski, J.; Ortiz, J. V.; Stefanov, B. B.; Liu, G.; Liashenko, A.; Piskorz, P.; Komaromi, I.; Gomperts, R.; Martin, R. L.; Fox, D. J.; Keith, T.; Al-Laham, M. A.; Peng, C. Y.; Nanayakkara, A.; Gonzalez, C.; Challacombe, M.; Gill, P. M. W.; Johnson, B. G.; Chen, W.; Wong, M. W.; Andres, J. L.; Head-Gordon, M.; Replogle, E. S.; Pople, J. A. *Gaussian 98*, revision A.7; Gaussian, Inc.: Pittsburgh, PA, 1998.

(29) Kasha, M. *Rev. Mod. Phys*. **1959**, *31*, 162.

(30) Kasha, M. *Rad. Res*. **1963**, *20*, 55.

(31) Kasha, M.; Rawls, H. R.; El-Bayoumi, M. A. *Pure Appl. Chem*. **1965**, *11*, 371.

(32) Gallos, L. K.; Pimenov, A. V.; Scheblykin, I. G.; van der Auweraer, M.; Hungerford, G.; Varnavsky, O. P.; Vitukhnovsky, A. G.; Argyrakis, P. *J. Phys. Chem. B* **2000**, *104*, 3918.

(33) Kodis, G.; Liddelle, P. A.; de la Garza, L.; Clausen, P. C.; Lindsey, J. S.; Moore, A. L.; Moore, T. A.; Gust, D. *J. Phys. Chem. A* **2002**, *106*, 2036.

(34) Clayton, A. H. A.; Scholes, G. D.; Ghiggino, K. P.; Paddon-Row, M. N. *J. Phys. Chem.* **1996**, *100*, 10912.

(35) Jeong, D. H.; Yoon, M.-C.; Jang, S. M.; Kim, D.; Cho, D. W.; Yoshida, N.; Aratani, N.; Osuka, A. *J. Phys. Chem. A* **2002**, *106*, 2359.

(36) (a) Greiner, S. P.; Winzenburg, J.; von Maltzan, B.; Winscom, C. J.; Moebius, K. *Chem. Phys. Lett.* **1989**, *155*, 93. (b) Fulton, R. L.; Gourterman, M. *J. Chem. Phys.* **1961**, *35*, *1059*; **1964**, *41*, 2280.

(37) (a) Burke, J. M.; Kincaid, J. R.; Spiro, T. G. *J. Am. Chem. Soc.* **1978**, *100*, 6077. (b) Hofmann, J. A., Jr.; Bocian, D. F. *J. Phys. Chem.* **1984**, *88*, 1472. (c) Seth, J.; Palaniappan, V.; Johnson, T. E.; Prathapan, S.; Lindsey, J. S.; Bocian, D. F. *J. Am. Chem. Soc.* **1994**, *116*, 10578. (d) Nakashima, S.; Taniguchi, S.; Okada, T.; Osuka, A.; Mizutani, Y.; Kitagawa, T. *J. Phys. Chem. A* **1999**, *103*, 9184.

(38) Kobayashi, H.; Kaizu, Y. In *Porphyrins*: *Excited States and Dynamics*; Gouterman, M., Rentzepis, P., Straub, K. D., Eds.; American Chemical Society Symposium Series 321; American Chemical Society: Washington, DC, 1986; p 105.

(39) (a) Chosrowjan, H.; Tanigichi, S.; Okada, T.; Takagi, S.; Arai, T.; Tokumaru, K. *Chem. Phys. Lett.* **1995**, *242*, 644. (b) Gurzadyan, G. G.; Tran-Thi, T.-H.; Gustavsson, T. *J. Chem. Phys.* **1998**, *108*, 385. (c) Mataga, N.; Shibata, Y.; Chosrowjan, H.; Yoshida, N.; Osuka, A. *J. Phys. Chem. B* **2000**, *104*, 4001.

(40) Kumble, R.; Palese, S.; Lin, V. S.-Y.; Therien, M. J.; Hochstrasser, R. M. *J. Am. Chem. Soc.* **1998**, *120*, 11489.

(41) Meier, T.; Chernyak, V.; Mukamel, S. *J. Phys. Chem. B* **1997**, *101*, 7332.

(42) Bakalis, L. D.; Knoester, J. *J. Phys. Chem. B* **1999**, *103*, 6620.

(43) Matyushov, D. V.; Voth, G. A. *J. Phys. Chem. A* **2000**, *104*, 6485.

(44) Mertz, E. L.; Tikhomirov, V. A.; Krishtalik, L. I. *J. Phys. Chem. A* **1997**, *101*, 3433.

(45) Even, U.; Magen, J.; Jortner, J.; Friedman, J.; Levanon, H. *J. Chem. Phys.* **1982**, *77*, 4374.

(46) Kakitani, T.; Kimura, A. *J. Phys. Chem. A* **2002**, *106*, 2173.

(47) Kimura, A.; Kakitani, T.; Yamato, T. *J. Phys. Chem. B* **2000**, *104*, 9276.

(48) Monshouwer, R.; Abrahamsson, M.; van Mourik, F.; van Grondelle, R. *J. Phys. Chem. B* **1997**, *101*, 7241

(49) van Oijen, A. M.; Ketelaars, M.; Köhler, J.; Aartsma, T. J.; Schmidt, J. *Science* **1999**, *285*, 400.

(50) De Boer, S.; Wiersma, D. A. *Chem. Phys. Lett.* **1990**, *165*, 45.

(51) Chachisvilis, M.; Kühn, O.; Pullerits, T.; Sundström, V. *J. Phys. Chem. B* **1997**, *101*, 7275.

(52) Pullerits, T.; Chachisvilis, M.; Sundström, V. *J. Phys. Chem.* **1996**, *100*, 10787.

(53) Förster, T. *Ann. Phys.* **1948**, *2*, 55.

(54) Förster, T. *Discuss. Faraday Soc.* **1959**, *27*, 7.

(55) Van Patten, P. G.; Shreve, A. P.; Lindsey, J. S.; Donohoe, R. *J. Phys. Chem. B* **1998**, *102*, 4209.

(56) Bilsel, O.; Rodriguez, J.; Milam, S. N.; Gorlin, P. A.; Girolami, G. S.; Suslick, K. S.; Holten, D. *J. Am. Chem. Soc.* **1992**, *114*, 6528.

(57) Petke, J. D.; Maggiora, G. M. *J. Chem. Phys.* **1986**, *84*, 1640.

(58) Ridley, J. E.; Zerner, M. C. *Theor. Chim. Acta* **1973**, *32*, 111.

(59) Orr, B. J.; Ward, J. F. *Mol. Phys.* **1971**, *20*, 513.

(60) Gouterman, M. *J. Chem. Phys.* **1959**, *30*, 1139.

(61) Rodriguez, J.; Kirmaier, C.; Holten, D. *J. Chem. Phys.* **1991**, *94*, 6020.

(62) Eom, H. S.; Jeoung, S. C.; Kim, D.; Ha, J.-H.; Kim, Y.-R. *J. Phys. Chem. A* **1997**, *101*, 3661.

(63) Yamaguchi, Y. *J. Chem. Phys.* **2002,** *117*, 9688.

(64) (a) Mukamel, S.; Tretiak, S.; Wagersreiter, T.; Chernyak, V. *Science* **1997**, *277*, 781. (b) Zojer, E.; Buchacher, P.; Wudl, F.; Cornil, J.; Calbert, J. Ph.; Brédas, J. L.; Leising, G. *J. Chem. Phys.* **2000**, *113*, 10002.

(65) Jeong, D. H.; Jang, S. M.; Hwang, I.-W.; Kim, D.; Matsuzaki, Y.; Tanaka, K.; Tsuda, A.; Nakamura, T.; Osuka, A. *J. Chem. Phys.* in press.

(66) Ong, K. K.; Jensen, J. O.; Hameka, H. F. *J. Mol. Struct.* **1999**, *459*, 131.

(67) (a) Siebrand, W. *J. Chem. Phys.* **1967**, *46*, 440. (b) Siebrand, W. *J. Chem. Phys.* **1967**, *47*, 2411.

(68) (a) Rao, D.; Aranda, F. J.; Roach, J. F.; Remy, D. E. *Appl. Phys. Lett.* **1991**, *58*, 1241. (b) Bezerra, A. G.; Borissevitch, I. E.; de Araujo, R. E.; Gomes, A. S. L.; de Araujo, C. B. *Chem. Phys. Lett.* **2000**, *318*, 511.

(69) Tsuda, A.; Nakamura, T.; Sakamoto, S.; Yamaguchi, K.; Osuka, A. *Angew. Chem.* **2002**, *41*, 2817.

(70) The directly linked orthogonal porphyrin arrays up to 128 Zn(II)-porphyrins connected together can be prepared. However, because of the relatively low solubility and the possibility of aggregation of longer arrays such as Z64 and Z128, Z48 was employed for electrical measurement in this study. For fused porphyrin arrays, Zn(II) porphyrin moieties can be fused up to 12 units (T12). However, because the longer fused array is more vulnerable to oxidation reaction, T8 was employed in our measurements.

(71) Park, H.; Lim, A. K. L.; Alivisatos, A.; Park, J.; McEuen, P. L. *Appl. Phys. Lett.* **1999**, *75*, 301.

(72) Liu, C.-Y.; Bard, A. J. *Electrochem. Solid State Lett.* **2001**, *4*, E39.

(73) The current at the voltage of 2.5 V for the fused porphyrin array is higher than that of the orthogonal porphyrin array by about 20 times, whereas the ratio of the length between orthogonal and fused porphyrin arrays is about 7. Consequently, the higher conductivity of the fused porphyrin array is not due to the length difference.

(74) Sheik-Bahae, M.; Said, A. A.; Wei, T.; Hagan, D. J.; van Stryland, E. W. *IEEE. J. Quantum. Electron.* **1990**, *26*, 760.